Theoretical and experimental study of paramagnetic semiconductors for cryogenic magnetic refrigeration

Aleksandr Vlasov

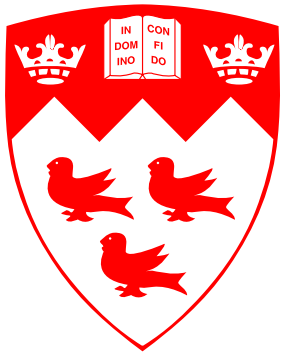

Department of Electrical Engineering
McGill University
Montréal, Québec, Canada

October 2018

Under the supervision of Professors Thomas Szkopek and Guillaume Gervais

---

A thesis submitted to McGill University in partial fulfillment of the requirements for the degree of Doctor of Philosophy.

Acknowledgments

This research work could not have been done without the support from my supervisor, Professor Thomas Szkopek, who provided guidance, resources and encouragement during the course of this project. He has been my mentor in scientific and creative thinking. I would like to thank him for his continuous financial support and research instruction during my thesis work.

I would like to acknowledge an invaluable help of my co-supervisor Guillaume Gervais who provided me with initial guidance in a field of low temperature physics and helped to avoid rookie mistakes. His experience in a field was crucial to make experimental part of this thesis.

I would also like to thank Pascal Pochet and Shengqiang Zhou for samples of neutron irradiated materials that were investigated in experimental part of this work. I am grateful to Don Pavlasek of the ECE Design and Machining facility who greatly helped me in design and manufacturing of the various custom parts required for experimental setups used through the research period.

Abstract

Recent advances in the development of quantum computing hardware, which typically operates at temperatures below 100 mK, motivates the search for new approaches and new materials for refrigeration at cryogenic temperatures. In this thesis, we present a theoretical and experimental investigation of paramagnetic semiconductors for cryogenic refrigeration by adiabatic demagnetization. Adiabatic demagnetization of paramagnetic salts has long been known as a means to achieve cryogenic refrigeration. The paramagnetism of semiconductors, introduced via doping or nuclear irradiation, can provide the entropy necessary for refrigeration. Unlike paramagnetic salts, semiconductors are environmentally stable and widely used in the manufacture of computing hardware.

The first part of this thesis includes a theoretical analysis of the refrigeration properties of various paramagnetic semiconductors, including Ge:As, Si:P, a-Si, 4H-SiC:N, neutron irradiated 4H-SiC, GaAs:Mn, GaN:Si, GaN:Mn and $Ga_{1-x}Mn_xN$. The model is based on experimentally measured heat capacity and magnetization data. We find that the paramagnetic entropy density of the dilute magnetic semiconductor $Ga_{0.9}Mn_{0.1}N$ is 48.4 $mJ/K\,cm^3$, which is comparable to the 11.1 $mJ/K\,cm^3$ density of the commonly used paramagnetic salt cerous magnesium nitrate hydrate (CMN). We extended our model to simulate the dynamic evolution of temperature versus time under the action of a swept magnetic field.

The second part of this thesis includes an experimental investigation of refrigeration with Si:P and neutron irradiated 4H-SiC. At an elevated tem-

perature range of 500 mK to 600 mK, a magnetic field swept at 50 mT/ min was observed to induce a cooling of 1.0±0.2 mK in Si:P and 5±2 mK in neutron irradiated 4H-SiC. Improved cooling performance is anticipated at lower base temperatures where parasitic heat capacity is minimized, and through the adoption of a heat switch for dynamic control over heat flow. Additionally, we report our experimental finding that the commonly used garolite fiberglass exhibits heating and cooling consistent with a paramagnetic entropy density of 0.1 $\mathrm{mJ/K\,cm^3}$. The source of this entropy has not yet been identified.

Abrégé

Les progrès récents dans le développement de matériel informatique quantique qui fonctionne généralement à des températures inférieures à 100 mK poussent la recherche de nouvelles approches et de nouveaux matériaux pour la réfrigération à des températures cryogéniques. Dans cette thèse, nous présentons une étude théorique et expérimentale de semi-conducteurs paramagnétiques pour la réfrigération cryogénique par démagnétisation adiabatique. La démagnétisation adiabatique des sels paramagnétiques est connue depuis longtemps comme un moyen de réaliser la réfrigération cryogénique. Le paramagnétisme des semi-conducteurs introduit par le dopage ou par l'irradiation nucléaire peut fournir l'entropie nécessaire à la réfrigération. Contrairement aux sels paramagnétiques, les semi-conducteurs sont stables dans l'environnement et largement utilisés dans la fabrication de matériel informatique.

La première partie de cette thèse comporte une analyse théorique des propriétés de réfrigération de divers semi-conducteurs paramagnétiques, tels que Ge:As, Si:P, a-Si, 4H-SiC:N, ainsi que 4H-SiC, GaAs:Mn, GaN:Si, GaN:Mn et $Ga_{1-x}Mn_xN$ irradiés par les neutrons. Le modèle est basé sur les données de la capacité thermique et de la magnétisation mesurées expérimentalement. Nous constatons que la densité d'entropie paramagnétique du semi-conducteur magnétique dilué $Ga_{0.9}Mn_{0.1}N$ est de 48.4 $\mathrm{mJ/K\,cm^3}$, ce qui est comparable à la densité de 11.1 $\mathrm{mJ/K\,cm^3}$ d'hydrate du nitrate céreux de magnésium de sel paramagnétique couramment utilisé. Nous avons étendu notre modèle pour simuler l'évolution dynamique de la température en fonction du temps sous l'action d'un champ magnétique balayé.

La deuxième partie de cette thèse comprend une étude expérimentale de réfrigération avec Si: P et 4H-SiC irradié par les neutrons. Dans une plage de températures élevées de 500 mK à 600 mK, il a été observé qu'un champ magnétique balayé à 50 mT / min induisait un refroidissement 1.0±0.2 mK dans Si: P et de 5±2 dans 4H-SiC irradié par les neutrons. On prévoit une amélioration des performances de refroidissement à des températures de base plus faibles, là où la capacité calorifique parasite est minimisée, et grâce à l'adoption d'un commutateur thermique pour le contrôle dynamique du flux de chaleur. De plus, nous rapportons notre découverte expérimentale selon laquelle la fibre de verre de garolite couramment utilisée présente un chauffage et un refroidissement compatibles avec une densité d'entropie paramagnétique de 0.1 $\mathrm{mJ/K\,cm^3}$. La source de cette entropie n'a pas encore été identifiée.

Statement of Originality

In this thesis, the following scholarly contributions are described:

1. We compare the specific heat contributions for different doped semiconductors, amorphous materials, irradiated semiconductors and semimetals. Our findings show that materials with the paramagnetic contribution dominating all other contributions are suitable for cryogenic refrigeration at very low temperature, T $\lesssim$ 1 K.

2. A cooling effect (reduction of temperature of the material in a changing magnetic field) was experimentally demonstrated in three materials:

   (a) A demonstration of cooling in phosphorus doped silicon (Si:P): in the order of 1 mK at a base temperature of 500 mK.

   (b) A demonstration of a cooling effect in neutron irradiated silicon carbide (SiC:n): in the order of 5 mK at a base temperature of 700 mK.

   (c) A demonstration of cooling in G10 garolite and an estimation of it's paramagnetic entropy density. A cooling effect of $\sim$ 100 mK was demonstrated at a base temperature of 500 mK.

3. Portions of Chapter 3 were published by the author of this thesis as *A. Vlasov, J. Guillemette, G. Gervais, T. Szkopek, "Magnetic refrigeration with paramagnetic semiconductors at cryogenic temperatures", Appl. Phys. Lett. 111, 142102 (2017).* Item 2(c) noted above is pending review by the McGill University Patent Office. Finally, a special report

regarding potential new approaches for cryogenic solid state cooling at the temperature around 20 mK was prepared for *D-Wave Systems*, the Canadian quantum computing company based in Burnaby, BC.

Contents

List of Tables

List of Figures

1 Introduction

This chapter presents the motivation for this work, summarizes the original contributions and gives an overview of the thesis structure.

1.1 Motivation

Adiabatic paramagnetic cooling achieves refrigeration through the exchange of entropy in a thermodynamic cycle. The exchange of heat by magnetization of spins was first observed in iron [1], and the magnetocaloric phenomenon was first applied to magnetic refrigeration by Giauque in 1933 [2]. The methods and practice of magnetic refrigeration have since been developed over many years [3], with the state-of-the-art involving the adiabatic demagnetization of electron spins in paramagnetic salt powders at the milliKelvin temperature scale, and nuclear spins in metals at the sub-milliKelvin temperature scale. There is currently a renewed interest in developing new methods and materials for cryogenic refrigeration, in large part driven by the development of new technologies such as quantum information processing [4, 5] which rely upon the generation of cryogenic temperatures.

As will be demonstrated in this thesis, there are classes of materials that would potentially push the limits for adiabatic cooling further down in temperature. Examples of interest are dilute magnetic semiconductors (DMS), where current research focus is on achieving high ordering temperature and current researches in phosphorus doped silicon, where the current area of interest is in the low doping regime and the creation of quantum memory and processors.

Other widely used milliKelvin cooling techniques (predominantly dilution refrigerators as described in detail in section 2) exist, but they require the use of the rare helium isotope ^{3}He. The ^{3}He isotope is extremely expensive because it is produced from the radioactive hydrogen isotope tritium ^{3}H, which in turn requires nuclear bombardment within a nuclear reactor to be produced.

We also note that ^{3}He can also be potentially used for aneutronic fusion - a fusion reaction with a negligible amount of released energy carried by neutrons. Both aforementioned factors keep demand and prices for ^{3}He extremely high, in the range of thousands of dollars per liter of gas at STP. This problem is known to the US government [6], with mining of the Lunar regolith being viewed as a potential solution for the production of ^{3}He.

One can conclude that any new cooling material or technology in the milliKelvin range would help mitigate the severe problem of ^{3}He and it's use in cryogenic experiments. Although existing paramagnetic salt powders have been previously shown to enable refrigeration at the milliKelvin range, utilization of these salts is not trivial. There are challenges for handling and thermal contacts, as will be shown in section 2.4. Moveover, they are not easily compatible with modern microelectronic foundries.

Lastly, the semiconductors that are proposed as new materials for adiabatic cooling in this thesis are the most common substrates used in electronic and micro-electromechanical (MEMS) devices. As such they offer the possibility of monolithic integration of a solid state refrigerant with active devices. Silicon is particularly appealing because of its wide availability and properties that are well understood but other materials should be considered as well.

Two recent experimental demonstrations of cooling in solid state device devices are noteworthy. One makes use of nuclear adiabatic refrigeration of a copper substrate to cool electrons and subsequently use these cold electrons within an electronic device [7]. Another experiment is a single electron transistor made of $Al_{98}Mn_2$ that demonstrated self-cooling during a magnetic field sweep [8]. However, both of these experiments achieve a cooling effect at the microscope scale, with scale-up to the macroscopic scale a non-trivial challenge.

1.2 Original contribution

A systematic study of potentially interesting new materials for adiabatic paramagnetic cooling is presented in this thesis, followed by an experimental demonstration and an estimate of cooling for three different types of materials: phosphorus-doped silicon (Si:P, a doped semiconductor), neutron irradiated silicon carbide (SiC:n, an irradiated semiconductor) and fibreglass (G10 garolite). The G10 garolite is manufactured by stacking multiple layers of glass soaked in epoxy resin, and compressing the resulting material under heat until the epoxy cures.

1.3 Organization

Chapter 2 describes an original theoretical model and the overview of projected refrigeration performance based on the published experimental data.

Chapter 3 describes a model for evaluation of efficiency of materials for adiabatic paramagnetic cooling and compares examples of materials from different classes against conventional paramagnetic salts used in cryogenics. Chapters 4, 5 and 6 present experimental results for three materials:

In chapter 4, cooling experiments with phosphorus-doped silicon (Si:P) are presented. A temperature change of 1 ± 0.24 mK was observed and confirmed with two different thermometry techniques. The same measurements were used to independently estimate the density of magnetic moments and these we have found consistent with previously published heat capacity measurements of Si:P. Chapter 5 describes cooling experiments with neutron irradiated silicon carbide (SiC:n). A temperature change of 5 ± 1.8 mK was observed and found larger in comparison with the < 1 mK cooling in pristine SiC. Chapter 6 describes cooling experiments with G10 garolite, an original "spin-off" experimental discovery of this work. A temperature change of $\simeq 100$ mK was observed. The final temperature reached was found to be below the base temperature achievable by the cryostat used in these experiments.

2 Literature review on cooling at milliKelvin temperatures

This chapter presents an overview of existing cryogenic cooling techniques relevant to the milliKelvin temperature range.

2.1 Gas based continuous cooling systems

Currently, ^{4}He based closed loop (dry or cryo-free) cryostats are standard cryogenic apparatuses. In this kind of system, ^{4}He is continuously condensed by heat exchange with an external cooling system, then passed to the main cryogenic chamber to cool a sample of interest. A pump is used to bring the vapor pressure of ^{4}He down to a few millibar, lowering the helium boiling temperature and further lowering the temperature to the range of 1 K. Such a system requires a very small amount of helium for it's functionality which is efficient and convenient for practical use. Closed loop systems operate in continuous mode providing an almost arbitrary amount of time at cryogenic base temperature.

Dilution refrigerators are much more complicated devices. The cooling power in such systems is based on the thermodynamic properties of a mixture of ^{4}He and ^{3}He at low temperatures: passing ^{3}He through the phase boundary of pure cold ^{3}He and a ^{3}He/^{4}He mixture is accompanied by a change of enthalpy and associated heat of mixing and thus leads to the removal of heat as in the case of evaporation. The main parts of a typical dilution refrigerator are shown in Fig. 2.1. Dilution refrigerators require complicated mixture, pumping, condensation and separation systems, with a detailed explanation found in [3]. Nevertheless, the simple ^{4}He system described above is always required as a first stage cooling system for dilution refrigerators. Typical dilution refrigerators have a base operating temperature in the range of $5 - 20$ mK.

Both systems mentioned above are continuous cycle systems, so low temperature can be maintained for an arbitrary amount of time and such systems can be used as pre-cooling stages for the single-shot cooling techniques described further below in section 2.3. The ^{4}He cryostat is a common place and standard experimental apparatus. The dilution refrigerator is the most common experimental apparatus for reaching temperatures of 20 mK and below.

2.2 Solid state based continuous cooling systems

The well-known Peltier thermoelectric effect and the rather less well-known Nernst-Ettinghausen thermoelectric effect can be used for continuous solid state cooling. Nowadays, the focus of this research area has shifted to the development of materials with high thermoelectric figure of merit at tempera-

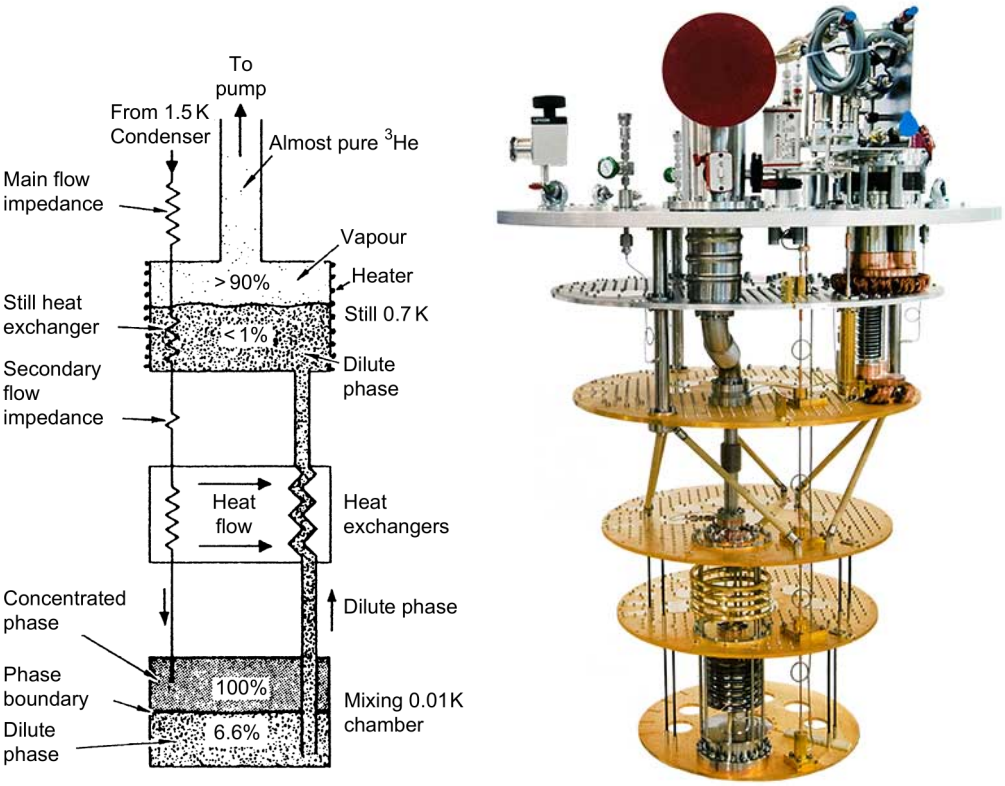

(a) (b)

Figure 2.1: a) Schematic ^{3}He – ^{4}He dilution refrigerator. The dilution refrigerator is placed in a vacuum chamber that is shielded from radiation and kept at 4K. The incoming ^{3}He gas is condensed on a continuously operating ^{4}He pot at 1.5K (image from [3]). b) Photograph of a complete dilution fridge low-temperature assembly (image from [9]).

tures above 300 K for energy recovery from industrial waste heat.

In the years ranging from 1950 to 1970, there was intense research in materials and techniques that would allow refrigeration to cryogenic temperatures without the usage of cryogenic liquids. Small-scale compressors and liquefiers for helium or nitrogen were not yet developed and widely adopted, so any system that would only consume electricity and maintain a low temperature for an arbitrary amount of time was of great interest at the time.

2.2.1 Peltier cooler overview

The Peltier effect is a continuous effect associated with entropy transfer by charge carriers. Here we give only a short overview of the material properties important for Peltier coolers. When current is passed through such a Peltier device, a temperature difference develops across the terminals of the device. The dimensionless material figure of merit for Peltier cooling is

$$ZT = \frac{S^2 T}{\kappa \rho}, \tag{2.1}$$

where S is the Seebeck coefficient of the material, effectively the entropy per charge carrier, T is the absolute temperature, κ is the thermal conductivity and ρ is the electrical resistance of the material. A material with $ZT > 1$ is considered suitable and effective for practical applications, and there are very few materials that satisfy this criterion. The ZT value determines the maximum temperature difference that can be achieved across the device terminals, and it also defines the thermodynamic efficiency of heat exchange in the device. A thermodynamic efficiency η of a Peltier cooler can be expressed

as

$$\eta = \frac{T_h - T_c}{T_h} \frac{\sqrt{1 + Z\bar{T}} - 1}{\sqrt{1 + Z\bar{T}} + T_c/T_h}, \tag{2.2}$$

where T_c is the cold side temperature, T_h is the hot side temperature, and $\bar{T}$ is defined as the average temperature between cold and hot sides of the device. A $ZT \to \infty$ limit corresponds to the Carnot cycle efficiency with the same cold side temperature T_c and hot side temperature T_h. Efficiency is especially important if the Peltier effect is used in one of the stages of a cooling system. A low efficiency will impose a larger heat load that itself must be removed by other stages in the cooling system.

With one side of a Peltier cooler thermally anchored, the maximum achievable temperature difference is

$$\Delta T_{max} = \frac{1}{2} Z T_c^2, \tag{2.3}$$

where T_c is the temperature of the cooled side of the device. This is only an upper limit to the temperature change because this relationship does not take into account Joule heating produced inside the device.

Another important property of a Peltier device is the power factor,

$$\mathrm{PF} = S^2/\rho. \tag{2.4}$$

In the context of cooling the power factor describes the ability of the material sustain a larger heat leak between terminals of the device for the same temperature difference between terminals. Some materials can have a large Seebeck coefficient value [10], although their electrical conductivity is also too

small for the efficient practical application. For example, in a low-doped semiconductor, the Seebeck coefficient value for electrons in the conduction band is described by Mott's formula

$$S_c = \frac{-k_B}{e}\left(\frac{E_c - \mu}{k_B T} + \alpha_c + 1\right), \tag{2.5}$$

where μ is the chemical potential in a semiconductor, E_c is the conduction band edge, and α_c is derived from the material's electrical conduction properties and is usually ranging from 1 to 3 for bulk low-doped semiconductors. As one can see at low temperatures, $S_c \to \infty$, even though the electrical conductivity exponentially drops to zero.

For practical applications, it is very difficult to find or engineer a material with high Seebeck coefficient, with low electrical resistivity and with low thermal conductivity. Notably, Bi based materials exhibit quite high ZT figure of merit [11, 12]. At much lower temperature, CeB_6 has the highest $ZT \sim 0.29$ around liquid ^{4}He temperatures [13]. Another promising material is $FeSb_2$, which has a gigantic Seebeck coefficient and a power factor at low temperatures is plagued by very high thermal conductivity [14]. It is believed by authors of [14] to be possible to substantially decrease thermal conductivity of this material at low temperatures without loss of other thermoelectric properties. There are no publications of successful results of such experiments yet.

One interesting approach to achieve a low temperature Peltier effect is to use the charge carrier spin degree of freedom as described in [15]. For example, continuous cycle cooling can be achieved by the exchange of spin entropy via a

spin current, leading to the spin Peltier effect. Cooling has been experimentally demonstrated in a mesoscopic device [16], spurring interest in the field of spin caloritronics [17]. Spin entropy is believed to play a dominant role in the large thermopower of the transition metal oxide $Na_xCo_2O_4$ at cryogenic temperatures [15].

In the low-temperature limit, the relation between thermal conductivity and resistivity is best described by the Wiedemann-Franz law

$$\kappa\rho = \frac{\pi^2}{3}\left(\frac{k_B}{e}\right)^2 T = L_0\, T,$$
$$L_0 = 2.44 \cdot 10^{-8}\ \mathrm{W\Omega K^{-2}},$$
$$ZT = \frac{S^2}{L_0}.$$

One can consider the contribution to the Seebeck coefficient from the spin degree of freedom absent of other entropy changes

$$S_{spin} = \frac{k_B}{e}\ln(2),$$
$$ZT = \frac{3\,\ln^2(2)}{\pi^2} \approx 0.15.$$

While this ZT value is very small, it is temperature independent, and can in principle be exploited at cryogenic temperatures. It will nevertheless converge to zero at $T \to 0$ as the entropy per charge carrier must converge to zero from the third law of thermodynamics.

As an example of modern advances in Peltier cooling, a six-stage device with a temperature difference of 136 K and hot side being kept at 350 K is

now commercially available [18].

2.2.2 Nernst-Ettingshausen cooler overview

The Nernst-Ettingshausen effect is a lesser known effect that can potentially be applied to cryogenic cooling. This effect can be described as the following: applying a current (along the y-axis) and a perpendicular magnetic field (along the z-axis) to a conductive material, a temperature gradient can be observed along the direction orthogonal to both current and the magnetic field (along the x-axis).

An effective infinite stage cooling device can be easily built by exponentially decreasing the width of the device along the direction of the temperature gradient [19],

$$z(x) = z(0)[z(L_x)/z(0)]^{x/L_x}.$$

Such devices were experimentally tested by various groups. As an example, a single stage device was used to attain a temperature of 200 K with the hot side anchored at 301 K [20]. Another experiment, now with the hot side being kept at 160 K, attained a temperature difference of 42 K [21] between the cold and the hot sides.

For a Nernst-Ettingshausen effect based cooler one can introduce a thermodynamic figure of merit $Z_{NE}T$ the same way as for Peltier effect based coolers. Here we only introduce it through the similar relation

$$\Delta T_{max} = \frac{1}{2} Z_{NE} T_c^2, \tag{2.6}$$

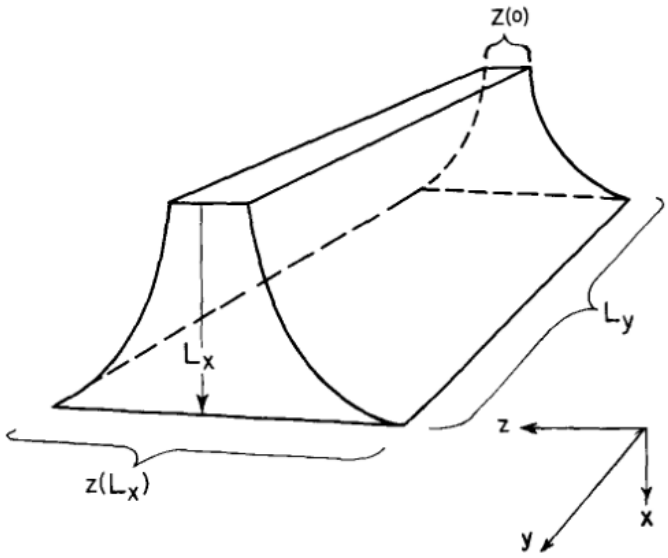

Figure 2.2: Infinite stage Nernst-Ettingshausen cooling device. Figure from [20].

where T_c is the temperature of the cooled side of the device. Recently a material with a high Nernst-Ettingshausen cooling figure of merit at the temperature of 1 K was found [22], however no direct experimental demonstration has been done yet, as the figure of merit was calculated from independent measurements of individual parameters.

2.3 Single shot cooling techniques and paramagnetic adiabatic cooling

The two approaches described above - continuous gas based techniques from section 2.1 and solid state effect techniques from section 2.2 - allow for a base temperature to be held for an arbitrary amount of time and can be used as a first cooling stage in single shot techniques, as discussed in this section.

In this thesis, two single shot techniques will be described in detail. These cooling approaches are the basis of the experimental work in this thesis. They are also the most widely used single shot techniques nowadays.

The first single-shot technique that we describe is the dipstick ^{3}He refrigerator. A small amount of ^{3}He gas (around 3 litres at STP) is contained in a sealed volume, consisting of an adsorbing material (usually charcoal). There is also a heat exchanger and a cold chamber with a plate that is only weakly thermally coupled to the heat exchanger. The operation principle and the main parts of this refrigerator are shown on a Fig. 2.3. The assembly is cooled by a ^{4}He based system and the sorb material is heated to keep the ^{3}He gas desorbed from the adsorption material (also called an adsorption pump). The heat exchanger is maintained below the ^{3}He boiling point 3.19 K, and condensed gas is accumulated in a cold chamber. After the accumulation of a sufficient amount of liquid ^{3}He the adsorption pump heating is turned off to allow it to cool, leading to adsorption pumping. This brings the temperature of the ^{3}He bath to around 300 mK. As the thermal link between the cold chamber and the heat exchanger (maintained at temperature around 2 K) is weak, the ^{3}He bath can be kept at a much lower temperature. This technique allows temperatures as low as $\sim$ 250 mK to be reached, and can typically be held for a time of approximately tens of hours. When all the ^{3}He is evaporated, there is no more cooling power available and the system warms up.

Another single-shot approach is the adiabatic cooling of paramagnetic spins. This approach achieves refrigeration on the basis of exchange of entropy during a thermodynamic cycle. The exchange of heat by magnetization

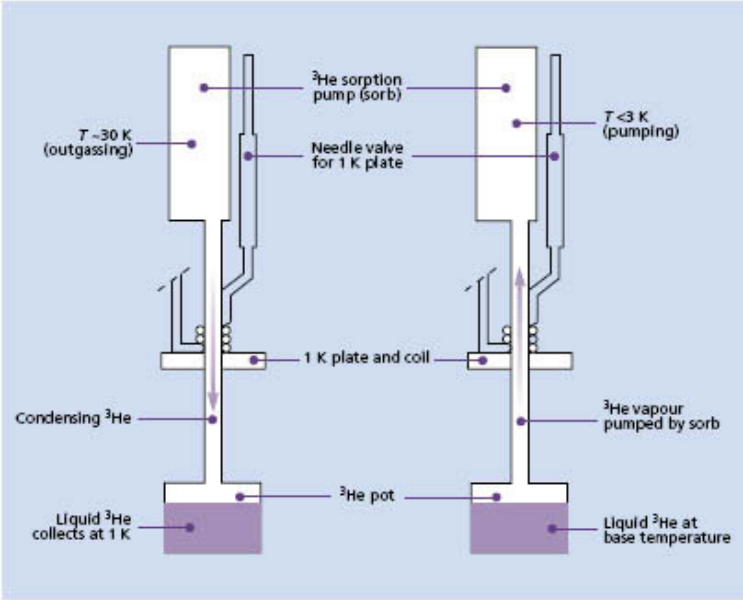

Figure 2.3: The operation principle of ^{3}He dipstick refrigerator. Figure from [9].

of spins was first observed in iron [1], and the magnetocaloric phenomenon was first applied to magnetic refrigeration by Giauque in 1933 [2]. The methods and practice of magnetic refrigeration have since been developed over many years and the underlying theory can be found elsewhere [3], with the state-of-the-art involving the adiabatic demagnetization of electron spins in paramagnetic salt powders at the milliKelvin temperature scale, and nuclear spins in metals at the sub-milliKelvin temperature scale. There is a currently renewed interest in developing new methods and materials for cryogenic refrigeration, in great part driven by the development of new technologies such as quantum information processing [4, 5] that rely upon the generation of cryogenic temperatures.

The thermodynamic cycle of a typical adiabatic demagnetization refrigeration cycle is shown in Fig. 2.4. Magnetic moments are polarized at a high field

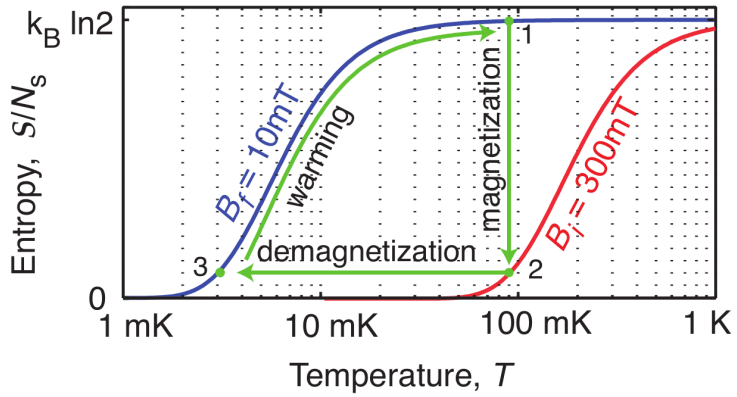

Figure 2.4: A typical adiabatic demagnetization refrigeration cycle.

B_i and at an initial temperature T_i to achieve a state of low entropy $\mathcal{S}(B_i/T_i)$. The initial temperature is reached by the use of an external cooling system, as mentioned above. An adiabatic sweep of the magnetic field to a final $B_f < B_i$ maintains constant entropy $\mathcal{S}(B_f/T_f) = \mathcal{S}(B_i/T_i)$, thus bringing the spins to a final temperature $T_f = T_i \cdot B_f/B_i$. The reservoir of low-temperature spins can thus be used as a refrigerant. To perform an adiabatic sweep it is necessary to break the thermal contact of the paramagnetic material with the external environment. This can be done by a heat switch. Finally, the sweep time should be small compared to the spin relaxation time, otherwise the spin polarization will be destroyed by its interaction with the lattice and itinerant electrons in the material.

In this work, a broad search of new paramagnetic materials was performed and several promising materials have been identified: doped semiconductors, irradiated semiconductors, and semimetals. This search is the subject of chapter 3.

2.4 Paramagnetic salts for demagnetization refrigeration

The desired physical properties for a paramagnetic salt to be used in magnetic refrigeration includes both magnetic properties, such as ordering temperatures and specific heat (both magnetic and other contributions), as well as general physical and chemical properties such as environmental stability, ease of handing and mounting and thermal conductivity. In this section, only the magnetic properties of the paramagnetic refrigerant will be reviewed.

The ideal material should have a low magnetic ordering temperature T_c which is the transition temperature from a paramagnetic state to a magnetically ordered state. The salt should have a large magnetic specific heat C_{magn} in order to achieve a large cooling power, which means a large angular momentum J and/or a high concentration of magnetic moments N_s. The ordering temperature T_c is itself determined by the interactions between magnetic moments. The paramagnetic specific heat should be large compared to phonon specific heat, which is usually the case at low temperature. The paramagnetic specific heat should also be large compared to the specific heat of free electrons, as will be discussed in section 3.2.

Salt	Chemical formula	T_c range	Entropy $\lim_{B\to 0} S/R$
MAS	$Mn^{2+}SO_4 \cdot (NH_4)_2SO_4 \cdot 6H_2O$	$\simeq 0.17$ K	ln 6
FAA	$Fe_2^{3+}(SO_4)_3 \cdot (NH_4)_2SO_4 \cdot 24H_2O$	$\simeq 0.03$ K	ln 6
CPA	$Cr_2^{3+}(SO_4)_3 \cdot K_2SO_4 \cdot 24H_2O$	$\simeq 0.01$ K	ln 4
CMN	$2Cr^{3+}(NO_3)_3 \cdot 3Mg(NO_3)_2 \cdot 24H_2O$	$\simeq 0.002$ K	ln 2

Table 2.1: Common paramagnetic salts used for refrigeration by adiabatic demagnetization. Data from [3].

As seen in the table 2.1, a higher magnetic moment J leads to a higher ordering temperature. This can be understood from the strength of the dipole-dipole interaction, $E_{d-d} \sim \mu^2/r^3$, where μ is the magnetic dipole moment and r is the distance between dipoles. Notably, all the paramagnetic salts used for refrigeration contain hydroxide groups and thus require careful treatment. The salt should not be exposed to the ambient environment and making a good thermal contact with paramagnetic salts is challenging.

2.5 Intermetallic compounds

New materials for adiabatic demagnetization are still being developed such as the intermetallic compound $YbPt_2Sn$ which combines a high specific entropy at $T < 2$ K together with metallic conductivity [23]. This material has an ordering temperature $T_c = 250 \simeq$ mK and a high density of magnetic moments, $N_s = 1.3 \times 10^{22}$ cm^{-3}, which is higher than in paramagnetic salts. Refrigeration has been demonstrated with a reduction of temperature from 1.45 K to 0.19 K using a magnetic field sweep from 6 T to near zero external field [23].

Another example of new materials as well as a new cooling approach has been demonstrated recently in $Yb_{1-x}Sc_xCo_2Zn_{20}$ [24]. Refrigeration was demonstrated from 1.5 K to 0.075 K using a magnetic field sweep from 8 T to near zero external field. In this material, a high-entropy super-heavy electron state is destroyed by the magnetic field, so that a magnetic field sweep from a high to zero field increases the entropy of itinerant electrons and hence absorbs heat.

3 New Materials for Paramagnetic Refrigeration

In this chapter we apply the theory of adiabatic paramagnetic cooling to compare the magnetic, phonon and electron contributions to specific heats for various semiconductor materials in an effort to identify several candidates appropriate for cryogenic refrigeration. The maximum extracted entropy per unit volume will be given for various doped semiconductors, irradiated and amorphous materials, along with a comparison with existing paramagnetic salts. At the end of the chapter, an important application of paramagnetic materials for low-temperature thermometry will be described.

3.1 Ideal model of adiabatic paramagnetic cooling

As mentioned in chapter 1, adiabatic cooling is described by the isentropic relation $\mathcal{S}(B_f/T_f) = \mathcal{S}(B_i/T_i)$, and the final temperature $T_f = T_i \cdot B_f/B_i$. There are two important points to consider with respect to the final field value:

- While $B_f \rightarrow 0$ is desired to achieve arbitrarily low temperature, this limit does not exist in practice because $B_f = \sqrt{B_{ext}^2 + b^2}$, where B_{ext} is the externally applied field (controlled in the experiment) and b is the internal field in the material arising from the magnetic moments in the material. In practice, the internal field gives a limit for the lowest attainable temperature in every material.

- The value of B_f also determines the amount of heat Q_{total} that can be extracted from the material during the transition from a fully polarized bath of magnetic moments to the equilibrium state of the magnetic moments, at a final temperature T_f and field B_f. In the case of a vanishing internal field, Q_{total}/B_f is a constant dependent on material parameters alone.

To understand the importance of various specific heat contributions, one can relate the total extracted heat during the warming of a paramagnetic material in B_f to the magnetic specific heat C_{magn},

$$Q_{total} = \int_{T_f}^{\infty} T \left(\frac{\partial S}{\partial T}\right)_{B_f} dT = \int_{T_f}^{\infty} C_{magn}\, dT, \tag{3.1}$$

where the latter follows from the relation between entropy and heat capacity

$$\left(\frac{\partial S}{\partial T}\right)_{B_f} = \frac{C_{magn}}{T}.$$

Without loss of generality, one can write the magnetic specific heat of a

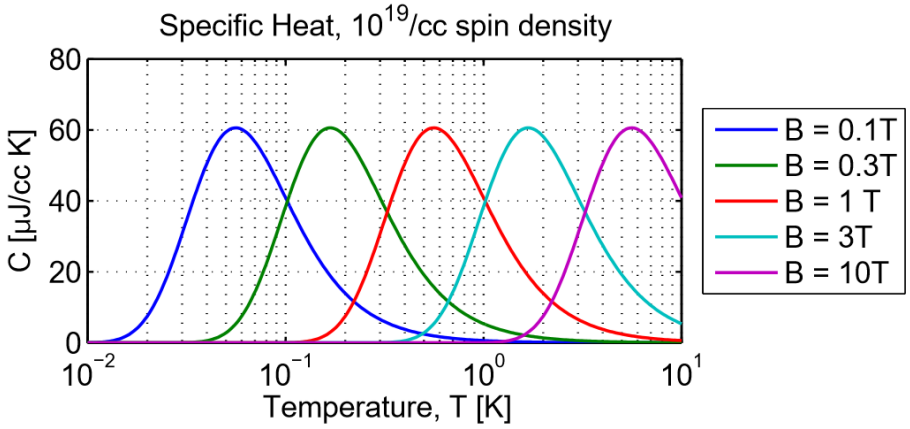

Figure 3.1: Specific heat in the presence of applied magnetic fields versus temperature for a total spin $J = 1/2$ and a Landé factor $g = 2$.

system of spin-1/2 moments with a Landé g-factor $g = 2$ as

$$C_{magn} = N_s k_B \left(\frac{\mu_B B}{k_B T}\right)^2 \operatorname{sech}^2 \left(\frac{\mu_B B}{k_B T}\right), \tag{3.2}$$

where k_B is the Boltzmann constant, μ_B is the Bohr magneton, B is the magnetic field, T is the absolute temperature, N_s is the spin (magnetic moments) density and the Landé g-factor $g = 2$ was numerically canceled in the equation. Consequently, the magnetic specific heat has a peak value at a particular value of the magnetic field,

$$\begin{aligned} C_{peak} &= 0.439 \cdot N k_B, \\ \left(\frac{B}{T}\right)_{peak} &= 1.20 \cdot \frac{k_B}{\mu_B}. \end{aligned}$$

Examples of specific heat curves for a magnetic moment concentration $N_s = 10^{19}\text{cm}^{-3}$ with spin-1/2 are presented in Fig. 3.1.

In the generally applicable case of a spin temperature T_f that is much less than the peak temperature T_{peak}, the total extracted heat can be integrated analytically,

$$Q_{total} = \int_0^\infty C_{magn}\, dT = JN_s|g|\mu_B B_f, \tag{3.3}$$

for the general case of a spin-J system with Landé factor g in external field B_f, and in the limit of a highly polarized state of the refrigerant ($k_B T_f \ll |g|\mu_B B_f$) prior to warming.

Formula 3.3 gives a good intuitive interpretation of absorption of the heat by the spin bath. The total absorbed heat Q_{total} is the energy needed to flip all the spins from a polarized state into a depolarized state as the spin system warms. Even though the integrals shown above have an upper integration limit in temperature of ∞, it is still a good approximation in the experimentally relevant situation where $T_f \ll T_{peak} \ll T_i$.

With the total amount of heat that can be absorbed by the *magnetic* subsystem as expressed above, the reduction in the temperature of a given experimental apparatus can then be determined by considering the total specific heat of the thermally coupled circuit. These sources of specific heat include:

- the sample of interest,
- parasitic contributions to specific heat arising from the mechanical structure and wires,
- the paramagnetic material itself, including contributions from the lattice and itinerant electrons, if present.

The last item in the list sets a limit for the performance of a magnetic

refrigerant and is thus the subject of immediate interest for the remainder of this chapter. In the extreme case of a paramagnetic material with large phonon specific heat, an experimental assembly (a paramagnetic material and some other device being installed for measurements) cannot be cooled effectively by demagnetization, as most of the absorbed heat will be expended in cooling the refrigerant's lattice. As such, the lattice final temperature will be larger than the final temperature of the magnetic subsystem, T_f.

Considering all of the points mentioned above, we can now make a list of the desired properties of a paramagnetic material optimized for cooling by demagnetization:

- A low specific heat contribution from phonons, which is easily satisfied at low temperature because $C_{phonon} \sim (T/\Theta_D)^3$, where Θ_D is the Debye temperature of the material.

- A low specific heat contribution from free electrons. This requirement is much stricter at low temperatures since $C_{elec} \sim T$ and an insulating material is preferred in order to avoid this contribution. In the case of doped semiconductors the itinerant electron contribution to specific heat is non-zero even at doping concentrations below the metal-insulator transition as will be shown in section 3.2.

- A high specific heat of the magnetic subsystem. There are several trade-offs to be considered in the choice of spin J, Landé g-factor, and spin density N_s. From formula 3.3 a high J is favorable, however a higher J leads to a higher ordering temperature. A high g may be desired, with

the g-factor determining the Zeeman splitting $g\mu_B B$, thus setting the relationship between field B and temperature T through the Boltzmann factor for spin polarization. A high spin concentration N_s is also favorable, but this also leads to a higher ordering temperature, and in the case of doped semiconductors, a higher doping concentration will yield a higher concentration of free electrons.

With all of these properties in mind, the next sections of this chapter will focus on a systematic comparison of existing experimental data so as to identify the most promising materials for adiabatic cooling.

3.2 Doped semiconductors

In this section, the paramagnetic properties of doped semiconductors will be discussed with a focus on the density of magnetic moments and the free electrons contribution to specific heat. Examples of specific heat for well-known and recently synthesized materials will be given.

Magnetic moments can be introduced into a non-magnetic semiconductor by impurity doping. The density N_s of impurity bound spins, which is critical to refrigerator performance as discussed in the previous section, itself depends upon the impurity dopant concentration N_D. At impurity dopant concentrations well below the critical density N_c of the metal-insulator transition (MIT), single electrons are bound to impurity dopants and then $N_s \simeq N_D$. As the impurity concentration approaches the critical density N_c, the spin density N_s exhibits a maximum before decreasing with increasing N_D. Experimental measurements of the specific heat in Si:P [25], electron spin resonance in Ge:As

and 4H-SiC:N [26], and electron spin resonance in GaN:Si [27], all show a rapid drop in spin density N_s as the dopant density approaches the critical density N_c.

The microscopic mechanisms responsible for the loss of paramagnetism as N_D approaches N_c varies from one material system to another. Antiferromagnetic ordering has been postulated in the form of singlet formation at doubly occupied donor sites [27] and singlet formation of spatially proximate donor sites [26, 25], per the theory of Bhatt and Lee [28]. From a thermodynamic perspective, the onset of spin ordering depletes the spin entropy that would otherwise be available for use in a magnetic refrigeration scheme. At doping densities N_D above N_c, electron delocalization reduces the density of localized electrons that contribute directly to paramagnetism. The Pauli paramagnetism of the delocalized electron gas above the MIT gives a very low magnetization, similar to the behavior of metals [29], and thus provides a negligible source of entropy S for magnetic refrigeration because the paramagnetic response becomes proportional to the dimensionless parameter $T/T_F \ll 1$, and $(\partial \mathcal{S}/\partial B)_T = (\partial M/\partial T)_B \sim 0$, where S is the entropy contribution, B is the magnetic field, M is the magnetization of the material.

3.3 Irradiated materials

Crystal lattice defects are another source of localized magnetic moments. An example of such a contribution to paramagnetism are dangling bonds on a surface or lattice vacancies in the bulk. Paramagnetism from localized electronic states can be introduced into semiconductors with structural defects.

Amorphous silicon is typically prepared in a hydrogenated state, a-Si:H, to passivate dangling bonds. The residual spin density is $N_s \sim 10^{16}\text{cm}^{-3}$ but can significantly be enhanced to a density $N_s = 6.3 \times 10^{18}\text{cm}^{-3}$ by thermal annealing to remove passivating hydrogen atoms and produce a-Si [30].

Neutron irradiation offers another alternative method of imparting paramagnetism. It has been shown that both semiconductors and semimetals exposed to neutron beams with different fluences lead to a variety of vacancies with a paramagnetic character. Irradiated samples can have a concentration of magnetic moments up to $N_s = 3.7 \times 10^{16}\text{cm}^{-3}$ under a neutron fluence of $N_n = 5.72 \times 10^{17}\text{n/cm}^{-2}$ [31]. Similar to doped Si, the magnetic moment density is not a monotonic function of the fluence and instead attains a peak value at a particular radiation dose. Irradiated Si has a magnetic moment of a μ_B per defect site. No ordering has been observed down to $T = 5$ K.

Similarly, samples of highly oriented pyrolytic graphite (HOPG) and silicon carbide (SiC) have been exposed to neutron radiation [32, 33]. The magnetic moment's density in HOPG reaches a striking value of $N_s(\textit{per unit mass}) = 8.0 \times 10^{19}\text{mg}^{-1}$ that is equivalent to $N_s = 1.82 \times 10^{23}\text{cm}^{-3}$ with g-factor of 2 and $J = 1/2$. No ordering was experimentally observed down to 1.8 K. In the case of 4H-SiC, it was also observed that neutron irradiation created a spin-1 density of $N_s = 5.3 \times 10^{19}\text{cm}^{-3}$. The paramagnetism is attributed to divacancies $\text{V}_{\text{Si}}\text{V}_{\text{C}}$ with a magnetic moment of $2\mu_B$.

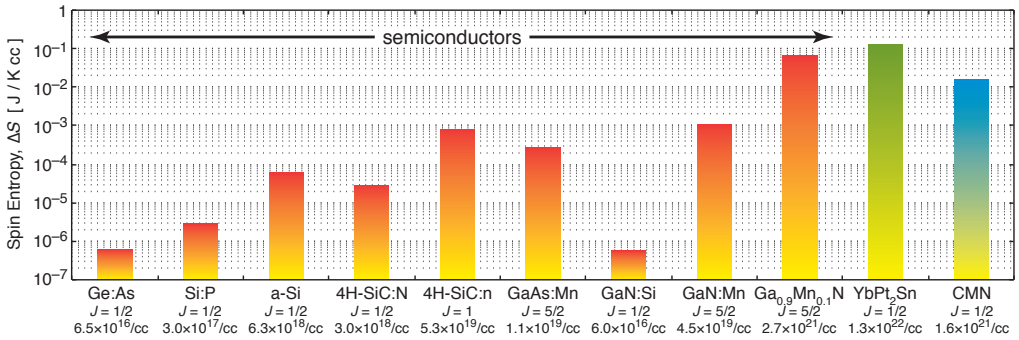

Figure 3.2: The theoretical spin entropy $\Delta\mathcal{S} = k_B N_s \ln(2J+1)$ of several semiconductor systems is compared along with the intermetallic compound $YbPt_2Sn$ [23] and the commonly used paramagnetic salt CMN [34]. The experimentally measured spin-J and spin density N_s are indicated for each material system. The semiconductor systems shown include Ge:As [26], Si:P [25], a-Si [30], 4H-SiC:N [26], neutron irradiated 4H-SiC [33], GaAs:Mn [35], GaN:Si [27], GaN:Mn [36] and $Ga_{1-x}Mn_xN$ [36].

3.4 Materials summary

In this section, a summary of the specific spin entropy $\Delta\mathcal{S} = N_s k_B \ln(2J+1)$ available for magnetic refrigeration for a variety of material systems is shown. A compilation is visually represented in Fig. 3.2, on the basis of the *experimentally measured* spin density N_s and angular momentum J.

Several common doped semiconductor systems are compared, including Ge:As [26], Si:P [25], 4H-SiC:N [26], GaAs:Mn [35], GaN:Si [27] and GaN:Mn [36]. Among these doped semiconductors, the general trend is that a greater spin density is achievable in larger gap semiconductors. The critical dopant density N_c at which electron delocalization occurs is very well approximated by $N_c = (0.26/a_B^*)^3$, $a_B^* = 1 - 100\,\text{Å}$ for a wide range of semiconductors [37], where a_B^* is an effective Bohr radius that tends to smaller values for larger

gap semiconductors and larger impurity ionization energies. In short, tighter confinement of localized states enables a greater density of localized states without the onset of delocalization. The critical density N_c parameter is known only for a subset of materials: Ge:As $3.7 \times 10^{17}\text{cm}^{-3}$, Si:P $3.77 \times 10^{18}\text{cm}^{-3}$, 4H-SiC:N $1.5 \times 10^{19}\text{cm}^{-3}$, GaN:Si $1.6 \times 10^{18}\text{cm}^{-3}$. Unfortunately, the critical doping density for GaN:Mn is unknown, as reported in [36], considering that even at 10% substitution there is a negligible density of free carriers.

Attention should be paid to the significant paramagnetism in dilute magnetic semiconductors (DMS) such as $Ga_{1-x}Mn_xN$ [36], where spin-5/2 paramagnetism of Mn at an effective concentration $x_{\text{eff}} = 0.061$ was observed in a crystal with Mn fraction $x = 0.096$. Anti-ferromagnetic coupling reduces the paramagnetism of magnetic semiconductors, but nonetheless enables a spin-5/2 density of $N_s = 2.7 \times 10^{21}\text{cm}^{-3}$ to be achieved. For comparison, a commonly used paramagnetic salt for magnetic cryo-refrigeration is cerous magnesium nitrate hydrate (CMN)[34], already described in section 2.4, where the Ce^{3+} ions have a spin-1/2 state and density of $N_s = 1.6 \times 10^{21}$ cm^{-3}. The magnetic semiconductor system $Ga_{1-x}Mn_xN$ gives a higher density of spins with a higher momentum J than that of CMN. It should be noted that magnetization curve for $Ga_{1-x}Mn_xN$ as measured experimentally and approximated by a Curie-Weiss law $\chi = \lambda/(T - \Theta_C)$ with Curie temperature Θ_C found to be negative from experimental fits indicates no immediate sign of ordering for temperatures down to 2 K. Therefore, $Ga_{1-x}Mn_xN$ is a promising candidate for further direct experimental cooling studies.

Interestingly, the specific example of $Ga_{1-x}Mn_xN$, which is a dilute mag-

netic semiconductor (DMS), demonstrates clearly that the current direction in magnetic materials research is focused on the synthesis of a material having ferromagnetic properties at room temperature, which is at the opposite extreme to the ordering behaviour required of magnetic materials for cryogenic applications.

3.5 Numerical simulation of cooling

To further illustrate the comparison noted above, the specific heat of three doped semiconductors were calculated on the basis of model parameters extracted from a variety of disparate experiments. A magnetic field $B = 0.1$ T as well as doping, spin and free electron densities are taken from published results. The impurity type, doping density and free electron density of the three doped semiconductor systems considered in detail are described below:

- Si:P at a P density $N_D = 1.0 \times 10^{18}\text{cm}^{-3}$ and corresponding spin-1/2 density $N_s = 3 \times 10^{17}\text{cm}^{-3}$ as measured by specific heat [25]. The free electron density was conservatively estimated as $n = N_D - N_s$. The basis for this estimate is the argument that localization length increases as the MIT is approached, and fluctuations in impurity density leads to an inhomogeneous distribution of localized and delocalized regions within a macroscopic sample. Both mechanisms contribute to free-electron like specific heat [25].

- 4H-SiC:N at an N density $N_D = 7.5 \times 10^{18}\text{cm}^{-3}$ and corresponding spin-1/2 density $N_s = 3.0 \times 10^{18}\text{cm}^{-3}$ as measured by electron spin resonance

[26]. The free electron density was estimated as $n = N_D - N_s$.

- GaN:Mn at an Mn density $N_D = 4.45 \times 10^{19}\text{cm}^{-3}$ and corresponding spin-5/2 density $N_s = N_D$ as measured by magnetization [36]. The free electron density was measured in the same samples to be $n \leqslant 1.0 \times 10^{18}\text{cm}^{-3}$.

The chosen magnetic field of $B = 0.1$ T corresponds to the final field B_f used further in a numerical simulation of adiabatic cooling for the same set of materials. The phonon specific heat was modeled as

$$C_{phonon} = (T/\Theta_D)^3,$$

where Θ_D is the Debye temperature of the material. The itinerant electron specific heat was modeled as

$$C_{el} \sim (T/\Theta_D)^3,$$

As one can see in Fig. 3.3, the specific heat of GaN:Mn is completely dominated by the spin contribution over a wide temperature range of interest (below 300 mK), while for Si:P the itinerant electron and spin contributions to specific heat are equal at ~ 220 mK. GaN:Mn will follow closely the behavior of an ideal paramagnetic system with negligible itinerant electron and phonon contributions to the specific heat in an adiabatic cooling cycle. In contrast, the Si:P temperature T versus field B dependence is expected to deviate strongly from the adiabatic limit of linear proportionality.

(a)

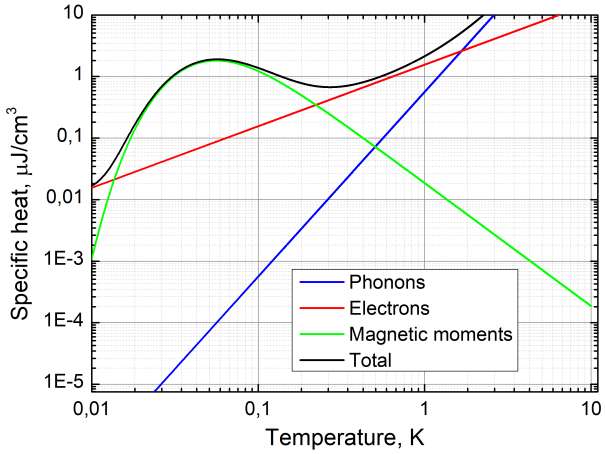

(b)

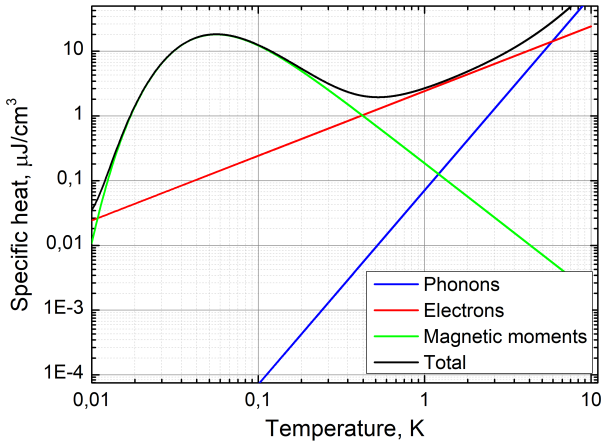

(c)

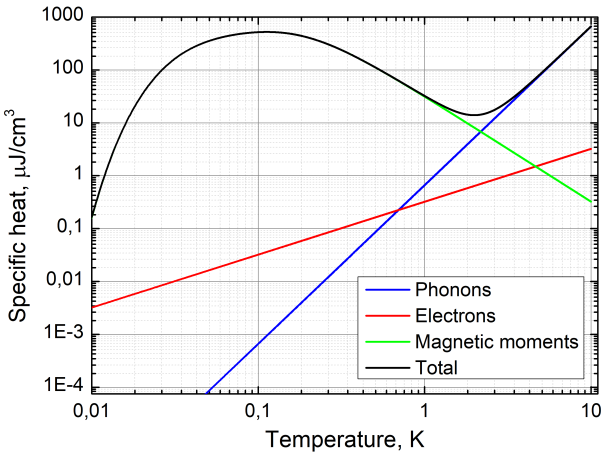

Figure 3.3: Specific heat for Si:P (a), 4H-SiC:N (b) and GaN:Mn (c) calculated based on experimental data for spin and free electron densities at the magnetic field $B = 0.1$ T. Details concerning doping and itinerant electron density assumed are given in the section 3.2.

Before introducing a time dependent simulation of temperature, it is important to note, that electron spin relaxation times T_1 in semiconductors can vary by many orders of magnitude, decreasing to short times in the case of heavily doped semiconductors. For example, $T_1 < 1$ s for $N_s > 10^{17}$ cm^{-3} in silicon [38]. Over the timescale of a demagnetization, typically of the order of 10^2 s to 10^4 s, the impurity spins and lattice phonons are effectively in thermal equilibrium, and a single temperature T describes the semiconductor lattice and spins. If spin relaxation is taken to be instantaneous, the rate of heat extraction $\dot{Q}$ from the environment by the semiconductor refrigerant is

$$\dot{Q} = T\dot{S} = T\left(\partial S/\partial B\right)_T \dot{B}. \tag{3.4}$$

In the case of the ideal spin-1/2 paramagnetic system, the heat extraction rate reaches a peak value of $\dot{Q}_{peak} = 0.448 \cdot N_s \mu \dot{B}$ at the magnetic field $\mu_B B_{peak} = 0.772\ k_B T$.

Using the parameters for Si:P, 4H-SiC:n and GaN:Mn as shown in a section 3.4, we construct a simple model to demonstrate the importance of specific heat contribution from magnetic moments. Assuming that the T_1 spin relaxation time is extremely short [38] for all these materials, including irradiated SiC, such that spin, electron and phonon temperatures are always in equilibrium, we model the magnetic refrigerant's temperature T during and after the magnetic field sweep from B_i to B_f with the differential equation

$$\dot{T} = \frac{T\dot{\mathcal{S}}}{C_{total}} - \frac{T - T_0}{C_{total}\, R_{th}}, \tag{3.5}$$

where $\dot{T}$ is the time derivative of the temperature, $R_{th} = \tau_{th}/C_0$, τ_{th} is the

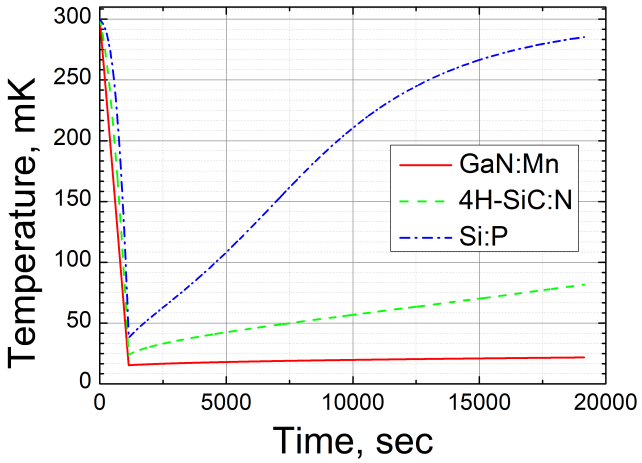

Figure 3.4: Simulated temperature versus time for Si:P, 4H-SiC:n and GaN:Mn using the model introduced in section 3.5. The base temperature $T_0 = 300$ mK, the initial external field $B_i = 2.0$ T, the final external field $B_f = 0.1$ T, the sweep rate is 0.1 T/min, and the thermal time constant $\tau_{th} = 1$ hour. Full time frame is shown to demonstrate the relationship between specific heat and hold time.

time constant for thermal relaxation processes near the base temperature T_0, and $C_0 = C_{electron} + C_{phonon}$ is the specific heat of the cooling medium in the absence of an externally applied magnetic field. This is in contrast with $C_{total} = C_{electron} + C_{phonon} + C_{spin}$, the specific heat including contribution from spins. The model is structured this way to separate the time constant τ_{th}, usually a cryogenic experiment design parameter, from C_{total} which varies during the magnetic field sweep from B_i to B_f. If $C_{electron} + C_{phonon} \ll C_{spin}$, then at final field B_f the effective time constant $\tau_{eff} = R_{th}/C_{total} \sim R_{th}/C_{spin}$ is larger. In addition, τ_{th} is expected to increase at a lower T due to a decrease in thermal conductivity. This would lead to a longer hold time at base temperature, but a specific model for this behavior is beyond the scope of this work.

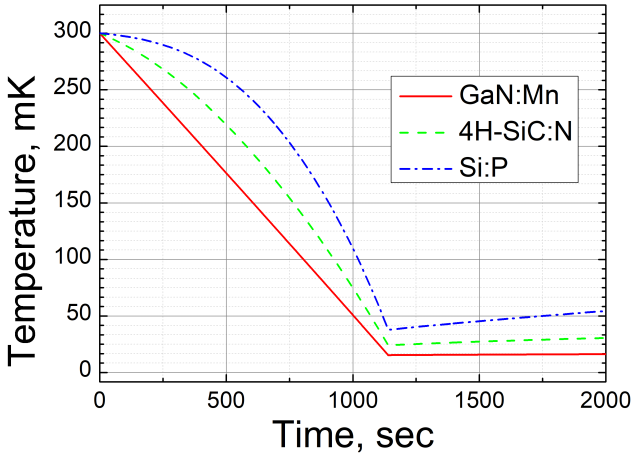

Figure 3.5: Simulated temperature versus time for Si:P, 4H-SiC:n and GaN:Mn using the model introduced in section 3.5. The simulation parameters are the same as for one shown on a Figure 3.4. Time frame of the magnetic field sweep is shown to demonstrate the relationship between specific heat and achieved temperature.

The time dependent results for the three semiconductors Si:P, 4H-SiC:n and GaN:Mn are shown on Figures 3.4 and 3.5, with two time scales presented : one for the full duration of the simulation and the other for the duration of the field sweep from B_i to B_f. The base temperature is chosen to be $T_0 = 300$ mK, and $B_i = 2.0$ T, $B_f = 0.1$ T, at a sweep rate 0.1 T/min and a thermal time constant of $\tau_{th} = 1$ hour. The initial conditions imply a sample that was already pre-cooled at a high field to the base temperature by an external cryogenic system. For the sequence of semiconductors Si:P, 4H-SiC:n and GaN:Mn, the spin contribution becomes more and more prominent, as indicated by a more linear T over B behaviour during the magnetic field sweep and increased hold time. The simulation of the GaN:Mn sample almost reaches a base temperature of 15 mK at B_f, as would be expected for a pure

magnetic system without any other contributions to the specific heat.

3.6 Thermometry application of paramagnetic materials

Another important application of paramagnetic salts is low-temperature thermometry. The magnetic susceptibility of a salt can be used to determine temperature from the Curie-Weiss law $\chi = \lambda/(T-\Theta_C)$ where λ is the material-specific Curie constant, and Θ_C is the Curie temperature. The temperature measurement range is limited by the ordering temperature $T \simeq \Theta_C$. Thus, new paramagnetic materials for adiabatic cooling also yield potential candidates for thermometry over the same temperature range.

One of the notorious problems at low temperature is establishing good thermal contact. Standard paramagnetic salt thermometers are electrically insulating and have low thermal conductivity. Consequently, it is difficult to thermally anchor a bulk paramagnetic salt sample. Specialized techniques are used to circumvent the low thermal conductivity of paramagnetic salts, such as the incorporation of metal wires inside a salt prior to compression and sealing. On the other hand, slightly conducting doped semiconductors such as those investigated in this thesis would have much higher thermal conductivity with a comparatively small trade-off in parasitic specific heat contribution from free electrons.

4 Experimental Demonstration of Refrigeration in Si:P

In this chapter, experiments demonstrating refrigeration in Si:P are described, as well as some important properties of a cryostat and of the superconducting magnet. Also, a model for isothermal sample mounting and different types of measurements will be explained. This will be followed by experimental measurements of Si:P. A cooling effect was observed, but it is presently too small to be of use and further work is required for applying Si:P in a magnetic refrigeration experiment.

4.1 Si:P sample properties and preparation

This section and subsequent ones cover the experimental procedures for near-isothermal cooling using precisely phosphorus doped silicon. Thermal properties of silicon vary greatly depending on the dopant nature and its concentration. In this work, commercially available silicon slabs from Virginia Semiconductor were used. The samples have a cylindrical shape with a 2.54 cm

diameter and 1 cm height, they are doped with phosphorus, and were cut in 5 pieces coming each from three different ingots. The room temperature resistivity is $0.01 - 0.02$ Ωcm, corresponding to a doping density on the order of 1.0×10^{18} cm^{-3}.

Based on experiments reported in Refs. [39] and [40], it is important to have a doping level below 2.0×10^{18} cm^{-3}, where specific heat measurements in an applied magnetic field clearly show a Schottky anomaly arising from localized moments. This is very important since cooling power is directly related to the specific heat of localized magnetic moments as discussed in chapter 3. In each of three doped silicon series, one piece was taken for resistance versus temperature measurements to ensure that samples were not overdoped above metal–insulator transition (MIT) limit. One sample was found to be metallic at low temperatures and from the remaining two the less insulating ingot was chosen for further measurements.

Five nearly identical pieces of the least insulating ingot were assembled into a stack using VGE-7031 varnish as adhesive. A thin layer of varnish was applied and the full assembly let to rest under force for 24 hours. One silicon piece in the stack has two cylindrical Al electrodes placed on its top surface. The 100 nm metal was deposited using a magnetron deposition system and was then annealed in a forming gas environment (H_2:N_2=1:20) at the temperature of 450 C for 30 minutes. The $I - V$ characteristics at 500 mK were measured and they show linear dependence within a bias range of ±0.2 V. In all further measurements, the excitation was never set beyond these values.

4.2 Experimental setup

4.2.1 Cryostat

All experiments were performed in an IceOxford Lemon cryogenic apparatus. It is a closed loop (dry) ^{4}He refrigerator that reaches a base temperature in the range of $1.2 - 1.7$ K, depending on the mode of operation. The system is equipped with two inserts, a variable temperature insert (VTI) probe and a ^{3}He insert. All experiments were performed using a ^{3}He insert that operates according to the principles previously described in chapter 2. There is a built-in calibrated Cernox thermometer mounted inside a cold plate in contact with the ^{3}He pot, which was typically held at 330 mK in the experiments reported here. The actual temperature achieved in experiments was 500 mK measured by ruthenium oxide (RuO_x) thermometers attached to the samples, and is higher because we purposefully included weak thermal links. Details pertaining to the thermometry are presented in a following subsection. The cold plate in contact with the ^{3}He pot is made of copper and has one M6 threaded hole in the middle of the plate and six M3 threaded holes in a circular arrangement.

During the experiment, the samples were mounted in two different ways:

- Large samples were directly coupled to the cold plate, using a support structure for mechanical stability. The copper plate was polished using a 2 μm diamond paste from THK and a thin layer of VGE-7031 varnish was applied to improve thermal conductivity and surface contact quality. Mechanical pressure was applied using a thin plate of G10 garolite mounted on two M3 threaded rods, made from non-magnetic 316 grade

stainless steel. Examples of the mounts are presented in sections 4.5 and 6.4. Mechanical pressure was not measured and ensured only mechnical integrity during the installation of an inset into the cryostat. In addition, to eliminate thermal contact there was no glue layer between samples and a thin plate that was used to apply pressure.

- For small samples, an additional support structure was manufactured. A slotted rod from coin silver ($Ag_{0.9}Cu_{0.1}$) was made, with an additional copper plate that allowed placement of the rod off-center. The coin silver rod was itself clamped mechanically to the cold plate using the central M6 threaded hole. Individual copper sample holders were clamped to the silver rod for mounting individual samples. An example of the mount is shown in section 5.2.

4.2.2 Magnet

The cryogenic apparatus is equipped with a superconducting magnet that allows reaching fields up to 8 T with a maximum sweep rate of 0.1 T/min. The cryostat and the magnet are optimized for efficient use of the helium and not for high sweep rate. The temperature change of the cold plate due to eddy current heating during the magnetic field sweep at the maximum sweep rate is approximately 1 mK and is usually less than typical cooling signals during the experiments. Larger temperature changes can occur during a sweep when the ^{3}He pot is almost depleted. The situation worsens if the additional copper plate for coin silver rod mounting is also present, although the cooling signals in experiments that required the installation of the coin silver rod were in order

of 5 mK.

4.2.3 Thermometry

Two types of thermometers were used in the experiments:

- *Bare chip ruthenium oxide thermometer.* Commercially available RuO_x thermometers model RX-102A-BR were purchased from Lakeshore Cryotronics. These thermometers have a working range 50 mK $-$ 40 K, they follow the standard curve, are available publicly, and have low magnetic field-induced errors. These thermometers have a typical size of $1.45 \times 1.27 \times 0.65$mm and they weigh less than 3 mg. This guarantees a negligible specific heat compared to the samples used as well as fast thermal response times. Two copper 36 AWG wires were attached to each thermometer using standard Sn60 ($Sn_{60}Pb_{40}$) solder. This solder becomes superconducting at 7 K, although the critical field is less than 0.1 T and hence the parasitic signal due to the superconducting transition occurs outside the relevant field range of our experiments.

- *Bare chip Cernox thermometer.* One Cernox CX-1030-SD-HT thermometer was used in the garolite G10 experiments of chapter 6. This type of thermometer is purchased uncalibrated, and comes without a standard curve. However, it was used only as a qualitative probe to confirm changes in temperature in the garolite G10 experiments. This thermometer is more massive (40 mg) and has two gold-plated copper leads soldered with the same Sn60 ($Sn_{60}Pb_{40}$) solder attached during manufacturing.

Bare chip ruthenium oxide RX-102A-BR and Cernox CX-1030-SD-HT thermometers are shown in Fig. 4.1.

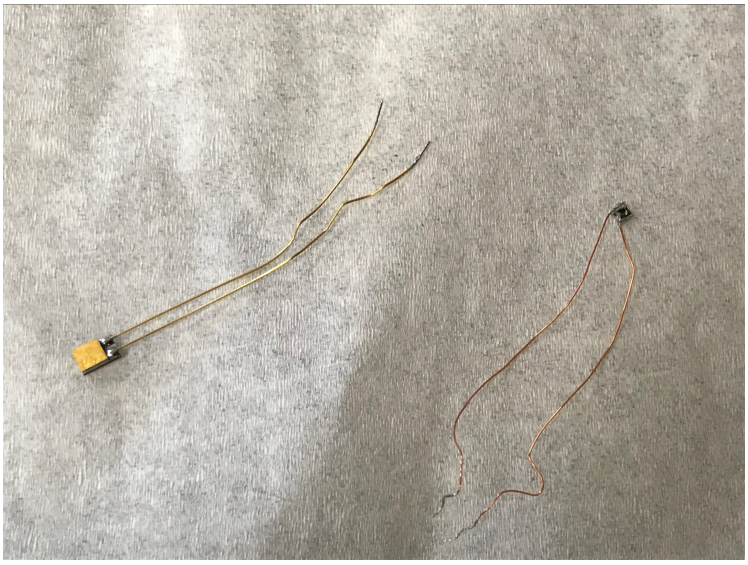

Figure 4.1: Zirconium oxy-nitride (Cernox, model CX-1030-SD-HT, left) and ruthenium oxide (RuO_x, model RX-102A-BR, right) thermometers, used in the experiment. RuO_x has copper leads attached for mounting, Cernox is used as purchased.

The thermometers were glued to the samples of interest by a thin layer of VGE-7031 varnish. To avoid a thermal short-circuit between the thermally anchored wire connector and the thermometers through the thermometer wiring, each thermometer was attached to the thermally anchored wire connector by at least 12 cm of AWG 36 resistive manganin wire. Two pairs (one to each copper lead as described above) were connected to allow for four-point measurement of thermometer resistance. Wires were mechanically fixed at intermediate points to prevent mechanical vibration that would otherwise cause heating.

The resistance measurements were performed using a lock-in amplifier. Most of the measurements were conducted with a Stanford Research Systems

SR830, with excitation set to 1 V, fed through a 10 MΩ resistor with precision rating ±1% forming a current source for the current leads. Typical thermometer resistances were in the range of $1 - 5$ kΩ, as measured from the voltage drop across the voltage leads, which is much less than the input impedance of 10 MΩ. The frequency was usually set in the range of $100 - 300$ Hz with an integration time of 1 second.

The ruthenium oxide thermometers show positive magnetoresistance and in some experiments the resistance values were corrected for magnetoresistance before transforming the thermometer resistance to temperature. Lakeshore Cryotronics publishes a relative temperature change $\Delta T/T = -1.4$ % for the 102A series of thermometers at a temperature of 2 K and a magnetic field value of 2.5 T with no further detail regarding changes of the differential sensitivity dR/dT. Thus for the purposes of thermometry in the experiments described below, a constant value of dR/dT was considered irrespective of the magnetic field.

For experiments requiring an additional DC bias to be applied to the thermometer as a source of external heat, a Stanford Research Systems SR124 lock-in amplifier was used.

The calibration of the RuO_x thermometers was additionally checked in a Bluefors dilution refrigerator. The built-in calibrated Cernox thermometer in Bluefors refrigerator was used as a reference. The comparison between experimentally obtained resistance versus temperature and the manufacturer supplied standard curves is shown in Fig. 4.2. During the calibration process, the same excitation parameters as those used in the refrigeration experiments

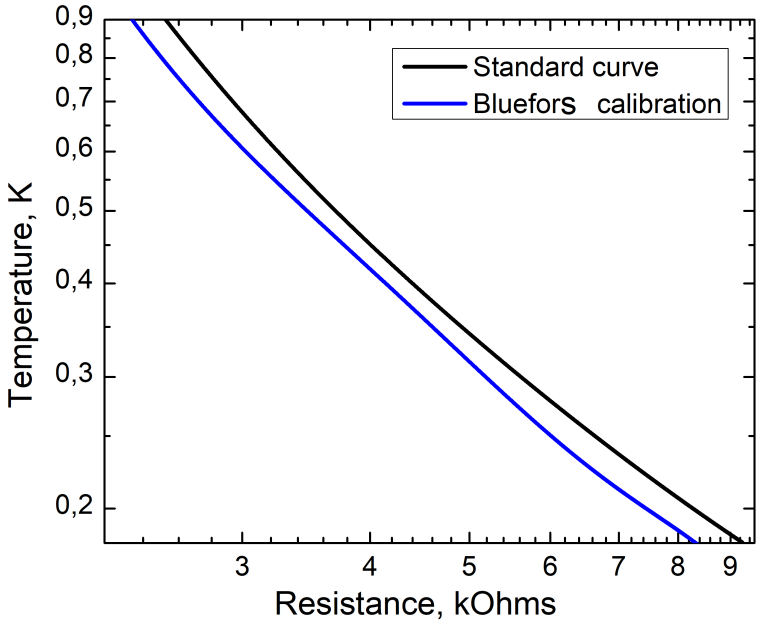

Figure 4.2: Ruthenium oxide (RuO_x, model RX-102A-BR) thermometer's publicly available standard calibration curve compared with resistance data obtained by mounting a thermometer on a cold plate of a dilution refrigerator.

were chosen (described as above). The experimentally obtained resistance for a given temperature is lower than the standard curve available for the thermometer can be explained by the thermal delay time between the thermometer and cold-plate reference thermometer during the continuous cooldown over which the data was acquired, so the cold plate was not in thermal equilibrium with the thermometer. Nevertheless, the calibration justifies the use of the standard curve provided by Lakeshore Cryotronics for all further transformations of RuO_x thermometer resistance readings to temperature.

It should be noted that over the time of experiments in the IceOxford Lemon fridge, the RuO_x thermometer base temperature (after initial cooldown

of ^{3}He pot) was never below 500 mK, even in a test experiment with only RuO_x thermometer being mounted in a direct contact with a cold plate, while the built-in cold plate thermometer indicated a temperature of 330 mK. The explanation of such discrepancy is beyond the scope of this work, although the most probable reason is an additional heat leak through the not well thermally anchored wiring posts on the ^{3}He insert. For all further purposes of the temperature measurements a value obtained from RuO_x was used, with the built-in thermometer used only to monitor a stability of ^{3}He pot temperature over the time of experiments.

4.2.4 Experiments at near iso-thermal conditions

As described in section 2, a heat switch is a crucial part for any adiabatic cooling experiment, allowing adiabatic cooling by breaking thermal contact with the external environment after initial cooling. Unfortunately, it was not possible to install such a heat switch in the cryostat, so instead a set of experiments based on the model described in section 3.5 was performed.

The temperature T of the magnetic refrigerant over time during a magnetic field sweep, assuming instantaneous spin relaxation, is expected to follow the differential equation,

$$\dot{T} = -\frac{T\dot{\mathcal{S}}}{C_{total}} - \frac{T - T_0}{\tau_{th}}, \tag{4.1}$$

where the dot on the variables denotes the time derivative, S is the magnetic entropy of the refrigerant, τ_{th} is the thermal time constant, T_0 is the equilibrium temperature of the paramagnetic material in the absence of the magnetic field sweep, and C_{total} is the effective specific heat of the material, including spin,

phonon and electron contributions as discussed in chapter 3. The minus sign in front of the first term indicates that when the entropy of the magnetic subsystem decreases with increasing magnetic field, the associated heat $T\delta S$ immediately warms up the lattice, and vice versa with a decreasing field.

It should be noted that the entropy S is a function of only the *absolute value* in the magnetic field $S(B) = S(|B|)$. Therefore, heat is released during an increase of the absolute value of the field, without any dependence on the direction of the externally applied magnetic field.

According to equation 4.1, producing a measurable temperature change in the paramagnetic medium requires that the thermal coupling $(T - T_0)/\tau_{th}$ should not cancel the entropy contribution to the temperature change $T\dot{\mathcal{S}}/C_0$. Thus, the following limits can be identified:

$$\tau_{th} \to 0,\ T \to T_0,\ \text{iso-thermal limit,} \tag{4.2}$$

$$\tau_{th} \to \infty, \frac{\dot{T}}{T} = \frac{\dot{\mathcal{S}}}{C_0},\ \text{adiabatic limit.} \tag{4.3}$$

In the absence of a change in entropy, if one supplies heat to the system by making use of an external heater, the steady-state condition is $T - T_0 = P_{ext}/R_{th}$, where P_{ext} is the external heating power, $R_{th} = C_0/\tau_{th}$ is the thermal boundary resistance, and C_0 is the specific heat without spin contribution.

4.3 Measurement procedures

Three types of experiments were conducted with near-isothermal mounting of the paramagnetic medium, described below.

1. **Continuous asymmetric sweep**

   In this kind of experiment a continuous sweeping of the magnetic field up and down was performed without crossing zero field. As described in section 4.2.3, a small amount of Sn60 ($Sn_{60}Pb_{40}$) solder undergoes a superconducting to normal first order transition in the magnetic field with associated with a release or absorption of heat. Some parts of the ^{3}He insert of the cryostat are also made of aluminum, and it also undergoes a similar transition in magnetic field. To circumvent this, during experiments continuous sweep in a field range $|B| > 0.15$T was performed as to avoid the field region of this transition.

   The experiment was controlled by an internally developed data acquisition software and the cryostat automation system. After cooling the ^{3}He pot cold plate to 330 mK by reading the built-in thermometer, the resistance of the thermometers attached to the sample were then monitored. After 30 minutes, or as soon as no changes on thermometer values were observed, the magnetic field was first ramped to the center of continuous sweep interval and then controlled to perform continuous sweeps of the kind $B_{min} \mapsto B_{max} \mapsto B_{min} \mapsto ...$. The reversal of the field sweep direction cannot be instantaneous and so for $\sim$ 5 seconds the sweep rate deviated from the set values at the end of each interval.

Sweeps were continued for at least two cycles until a steady state loop of thermometer resistance versus magnetic field developed. The difference in thermometer resistance during positive $d|B|/dt > 0$ and negative $d|B|/dt < 0$ sweeps, when plotted as $T\ vs\ B$, was used to define a loop opening. Simultaneously, the ^{3}He pot cold plate temperature was monitored by the built-in cryostat thermometer, assuring that the magnitude of the loop opening on the ^{3}He pot thermometer is negligible compared to the loop opening of the sample thermometer. The typical size of the loop on ^{3}He pot thermometer was in the range of ~ 1 mK.

A continuous sweep in both directions improved the signal to noise ration two-fold, as the temperature on a sweep up in $|B|$ caused $\dot{Q} = T\dot{\mathcal{S}} > 0$, whereas sweeping back down provides $\dot{Q} < 0$ with a similar magnitude as described by Eq. 3.4.

2. **Continuous symmetric sweep**

   To confirm the absence of explicit dependence of the observed heat exchange on the magnetic field orientation (i.e. no hysteresis loop due to any partial magnetic ordering or other artefacts), sweeps in a range ± 2 T were performed for the G10 sample.Spurious temperature changes around 0.1 T are clearly visible on these sweeps as parasitic heat is released in the cryostat and thermometry solder.

3. **Thermal boundary resistance measurements**

   In experiments with two thermometers attached to the sample, one thermometer was used as a heater by application of small DC bias on top of

AC excitation from the lock-in amplifier to simultaneously provide heat dissipation and simultaneously measure the resistance value. The temperature difference at equilibrium allows us to estimate the parameters used in thermal boundary resistance $R_{th} = P_{ext}/(T - T_0)$ where P_{ext} is the external heating power applied through one of the thermometers, T is the steady-state temperature when external heating is applied, and T_0 is the steady state temperature in the absence of external heating.

4.4 Estimation of the magnetic moments density

The estimation of the magnetic moments density is important to check the self-consistency of experiments by comparison with data from published results. One can simplify Eq. 4.1 described in section 4.2.4 by assuming that the timescale for variation in $\dot{S}$ due to the magnetic field change $|\dot{B}|$ is much larger than τ_{th}. Then, a variation of the temperature of the sample $\delta T = T - T_0$ is always at equilibrium, and given by

$$\delta T \simeq T_0 \dot{S}/R_{th}. \tag{4.4}$$

Half of the maximum opening of the loop in this case corresponds to a power

$$\dot{Q}_{peak} = 0.448 \cdot N_s \mu \dot{B}, \tag{4.5}$$

yielding an estimate for N_s, in this case for a spin 1/2 system.

4.5 Sample mounting

The assembly described in the section 4.1 was directly attached (glued) to the plate of ^{3}He pot on IceOxford Lemon cryostat and clamped from the other side by thin G10 garolite plate supported between two M3 nonmagnetic stainless steel rods. Two RuO_x Lakeshore RX102-A thermometers were attached to the top and bottom silicon pieces in a stack with wiring installed as described in the corresponding section of 4.2.3. Full assembly is shown in Fig. 4.3.

The assembly was cooled to the base temperature of 330 mK according to a permanent built-in thermometer placed in the ^{3}He plate. Various parameters for sweep rate and the magnetic field range were chosen to confirm that any observed cooling effect doesn't depend on the direction of the magnetic field. In addition, the same thermometers were detached from silicon stack and placed directly on ^{3}He plate and measured under the same field parameters used during measurements with the silicon stack. There was no observable loop in thermometer resistance under asymmetric field sweeping conditions when the thermometers were mounted alone on the cold plate.

During the magnetic field sweeps the resistance of the two thermometers were recorded and transformed to temperature according to the standard calibration curve from Lakeshore. As an independent measure, simultaneous capacitance measurement between two annular electrodes on the top silicon piece in the stack was taken by an Andeen Hagerling AH-2550A capacitance bridge at a frequency of 1 kHz. The temperature of the sample was taken from direct application of calibration curve to the ruthenium oxide thermometer resistances.. During the cooldown from 530 mK to 500 mK (region of all further

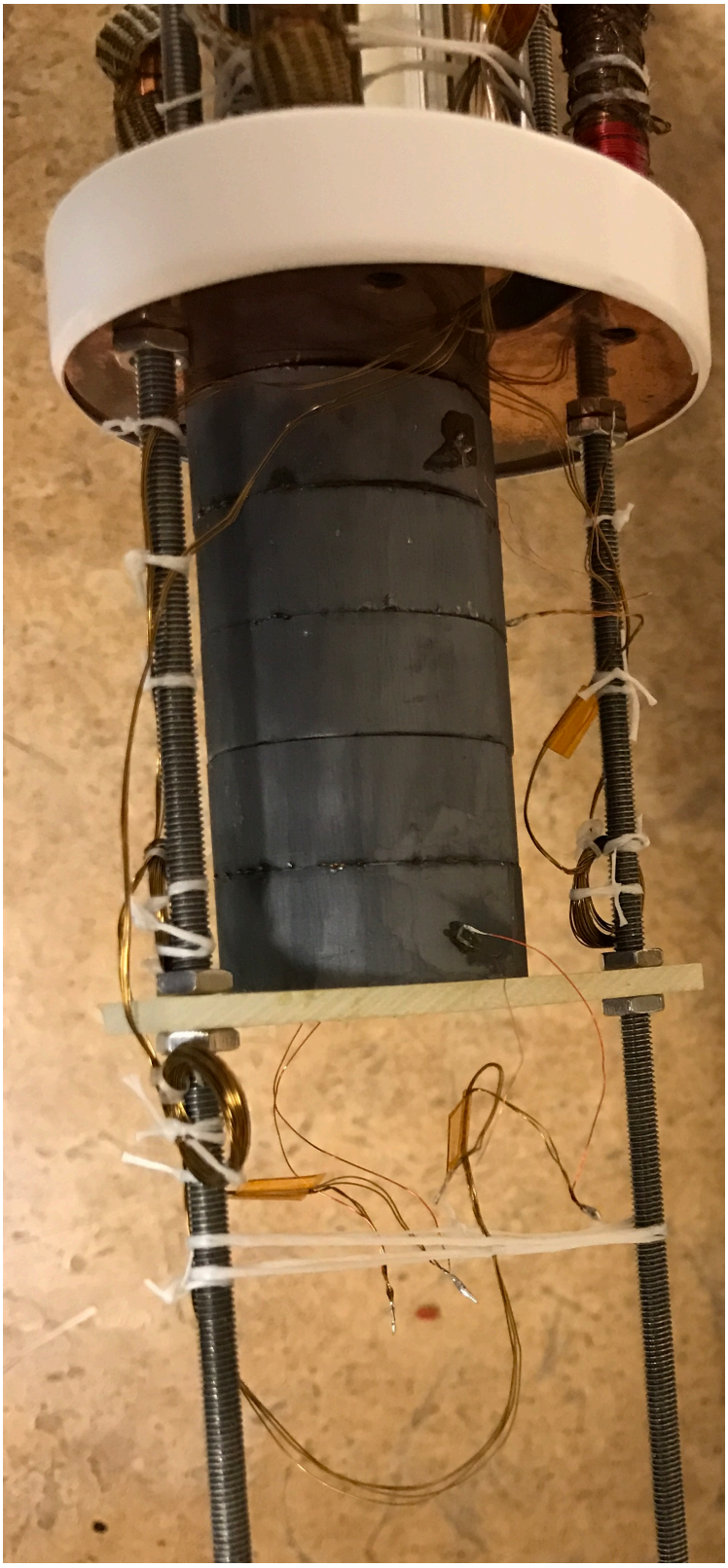

Figure 4.3: Phosphorus doped silicon (Si:P) mounting setup.

temperature variations), the capacitance versus temperature dependence is linear and the linearity coefficient was used to transform capacitance difference during the sweep into temperature difference. The capacitance calibration curve is shown in Fig. 4.4.

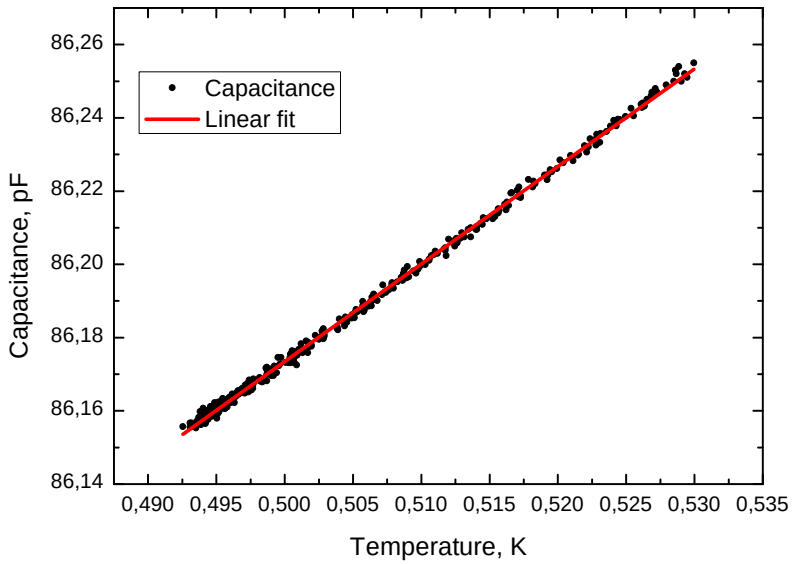

Figure 4.4: Capacitance calibration in phosphorus doped silicon (Si:P) cooling experiment.

4.6 Experimental results

Due to the near-isothermal mounting of the silicon stack and the low reported concentration of magnetic moments the resulting cooling signal was expected to be very small, so the range of magnetic field values was chosen to demonstrate cooling effect where it is expected to be largest: field range from 0.15 T to 0.45 T and sweep rates of 0.1, 0.05 and 0.025 T/min. This mag-

netic field range is beyond all potential superconducting transitions within the cryogenic system and mounts, such as solder joints and aluminum parts and is narrow enough not to be affected by long-term temperature drifts inherent to the cryogenic apparatus. As mentioned before, 0.1 T/min is a maximum sweep rate achievable with the 8 T superconducting solenoid.

The slowest sweep rate was used to calibrate capacitance change versus magnetic field. The change of capacitance with magnetic field is expected as a reflection of the Kramers–Kronig relation applied to magnetoresistance - in a formalism of complex conductivity a dielectric permittivity is an imaginary part of complex conductivity, thus any change in electrical resistance should result in a change of dielectric permittivity and measured capacitance. A continuous sweep with low constant rate was chosen for the calibration due to the non-negligible effect of eddy current heating in the ^{3}He pot copper mounting plate. The resulting magnetocapacitance calibration curve is shown in Fig. 4.5.

During the field sweeps at rates 0.1 and 0.05 T/min the silicon capacitance and RuO_x thermometer resistances were recorded. Figures 4.6a and 4.6b show corresponding silicon temperature versus magnetic field estimated from capacitance changes and thermometers resistances respectively. The reference silicon capacitance and thermometer resistance was taken at $B = 0.15$ T with a 0.025 T/min sweep rate. The absolute value of the effect was estimated from RuO_x temperature and from capacitance changes over the duration of a sweep are different however both methods for *in situ* temperature estimation agree with the presence of a temperature loop during field sweeping.

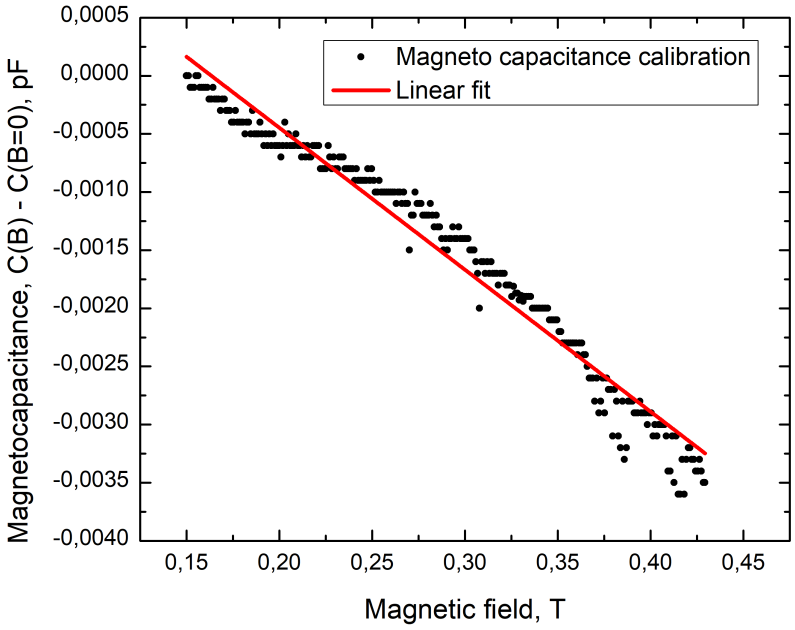

Figure 4.5: Phosphorus doped silicon (Si:P) magnetocapacitance calibration.

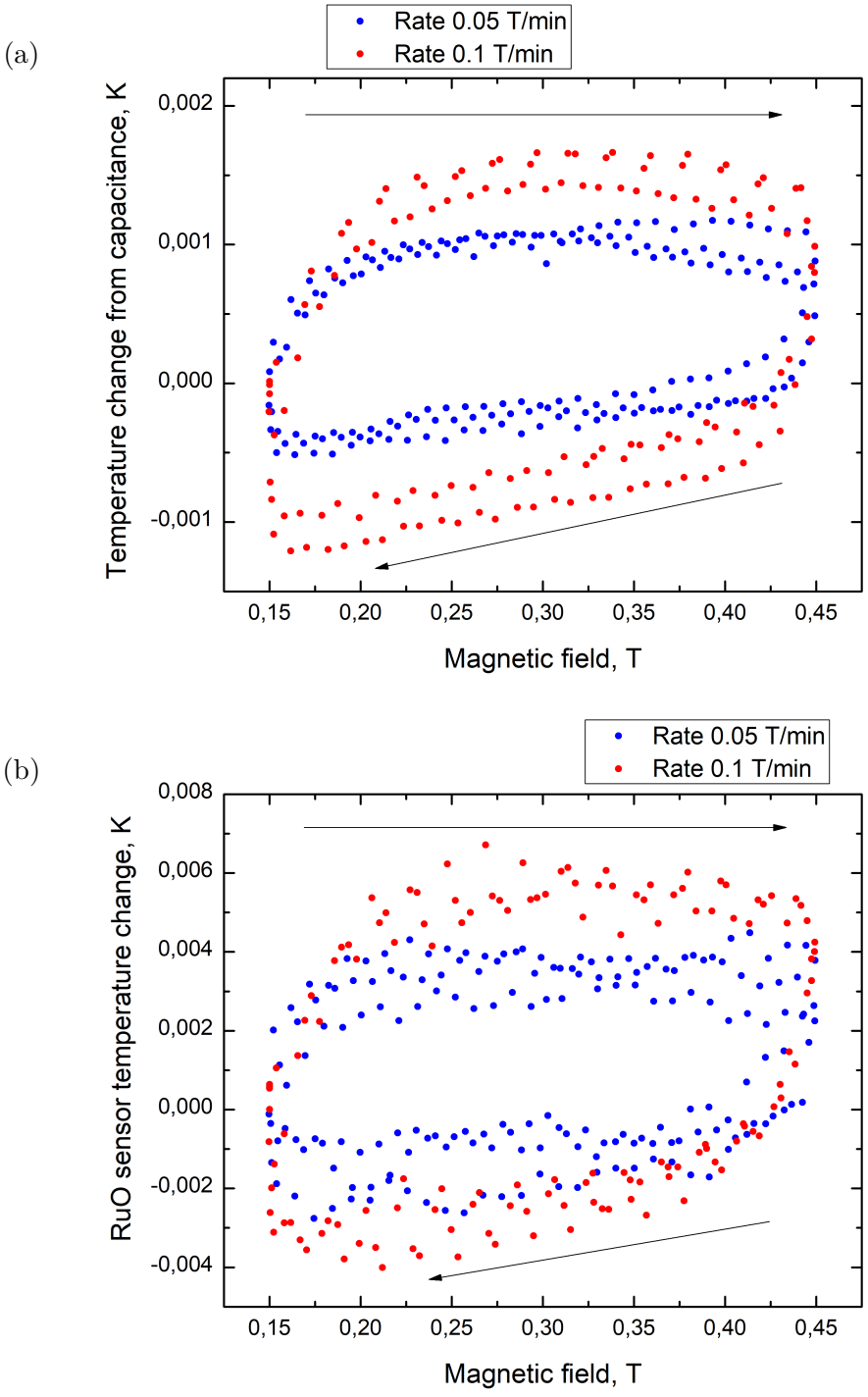

Figure 4.6: Si:P sample cooling effect: a) estimated from capacitance change b) from thermometry. Range of resulting values is different for two methods and scale of both plots is chosed for visual guidance. In the text of the thesis quantitative results are presented for direct thermometry.

$1.4 \pm 0.2 \times 10^4 \ \frac{\mathrm{K}}{\mathrm{W}}$.

The resulting heating/cooling effect magnitude and Eqs. 4.4 and 4.5 from section 4.3 allow us to estimate the spin density in the sample. For this estimate, the average cooling power for a sweep rate of 0.1 T/min and $B = 300$ mT was used together with a corresponding temperature change due to the magnetic field sweep of 1 ± 0.24 mK. For these values, the resulting spin density for the investigated series of silicon samples is estimated to be $4.0 \pm 1.1 \times 10^{17}$ cm^{-3}. According to Ref. [39], such spin density is expected for doping concentrations in the range of $0.53 - 2.7 \times 10^{18}$ cm^{-3}, in agreement with the dopant densities in the silicon used in this experiment.

Over the course of experimental research of Si:P at least 6 experiments were performed based on the number of data files that were used for data analysis.

4.7 Conclusion

A cooling effect was demonstrated for phosphorus-doped mono-crystalline silicon. The sample qualitative behavior in the near-isothermal mounting regime agrees with a simple model The silicon temperature was independently estimated by silicon capacitance measurement and by external resistive thermometry. An estimation of the density of magnetic moments agrees well with the expected values previously published in Ref. [39]. The absolute value of the cooling effect is small and is not yet sufficient for day to day applications of solid state cooling.

5 Irradiated SiC experiment

Following a recent discovery of induced paramagnetism [31, 32, 33] in various materials, samles of neutron irradiated samples of silicon, graphite and silicon carbide were obtained thank to invaluable help of Dr. Zhou Shengqiang from Helmholtz-Zentrum Dresden-Rossendorf, Institute of Ion Beam Physics and Materials Research, Dresden, Germany, along with pristine (non-irradiated) SiC samples. High spin-1 magnetic moments density $N_s = 5.3 \times 10^{19}\text{cm}^{-3}$ in 4H-SiC was worth investigating experimentally for cooling purposes. The obtained samples are thin $\sim$ 0.5 mm plates with approximate 3×4 mm lateral dimensions. During the experiment a cooling effect was observed for irradiated SiC samples compared to pristine SiC.

5.1 Sample properties and preparation

The exact information about irradiation of every type of material is described in original sources [32, 31, 33]. In total four samples were investigated experimentally with radiation exposure times described in Table 5.1. For con-

sistency, samples with maximum irradiation time were chosen, even though it may not have been an optimal choice for silicon. A piece of pristine SiC also allowed us to compare irradiated and non-irradiated samples for this material in particular.

Material	Neutron radiation exposure time
Si	150 hours
HOPG	150 hours
4H-SiC	120 hours
4H-SiC	-

Table 5.1: Radiation exposure times for investigated material samples.

5.2 Sample mounting

To mount the samples, copper T-shaped holders were fabricated with a small fork-shaped gold-plated beryllium copper leg glued to the end. Holders were clamped to the silver rod as described in section 4.2.1. Individual RuO_x thermometers were glued to the samples with VGE-7031 varnish. Each sample was placed between the legs of the fork-shaped holder and fixed in place with a minimal amount of VGE-7031 varnish. All four mounted samples are shown in Fig. 5.1.

The experimental setup was placed in a cryostat and cooled down to the base temperature of 330 mK according to the built-in thermometer on ^{3}He plate. The thermal resistance allows the swept magnetic field experiments to be conducted in a regime that is intermediate between the adiabatic limit, where thermal resistance is infinite, and the iso-thermal limit, where thermal

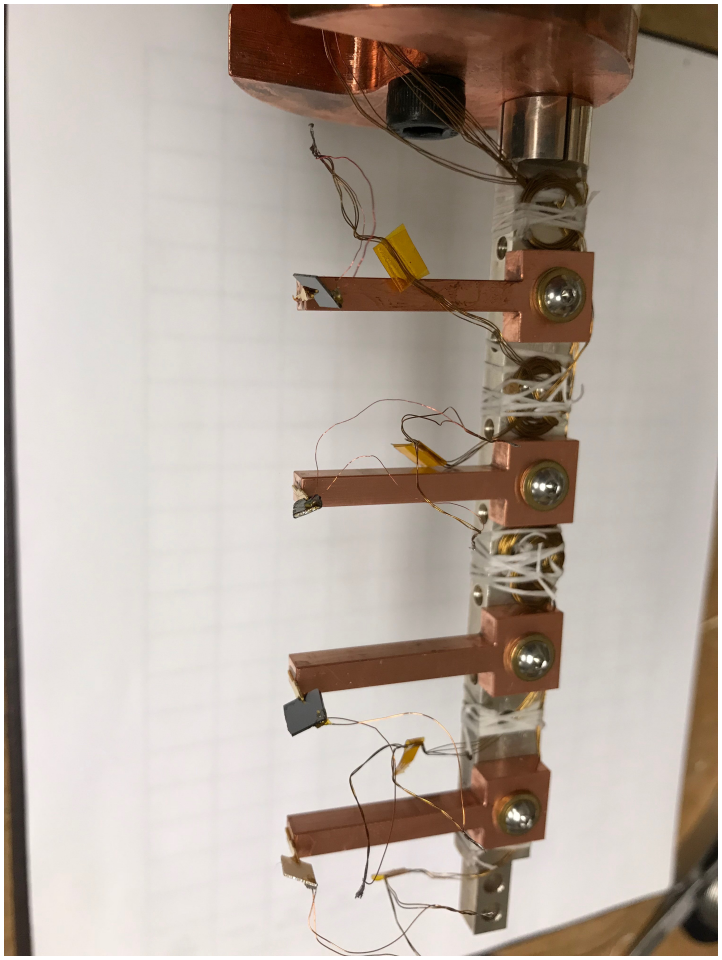

Figure 5.1: Mounting of irradiated samples for the first experiment. Samples of irradiated silicon, graphite and silicon carbide, as well as pristine silicon carbide are mounted (from top to bottom).

resistance is zero. An ideal experiment uses a heat switch between these two regimes of thermal contact with the ^{3}He reservoir. In our experiments, a constant thermal resistance was employed. The thermal resistance must be sufficiently low to allow the samples under test to be pre-cooled to a sufficiently low temperature where paramagnetic entropy is sufficiently large to enable cooling. Simultaneously, the thermal resistance must be sufficiently high to prevent sample temperatures from being anchored to the temperature of the cold plate.

To search for an additional evidence of the cooling effect, an experiment was repeated with a slightly modified mounting assembly and an improved uniformity of thermal coupling between different samples and ^{3}He pot cold plate, that resulted in closer base temperature values for samples of pristine and irradiated SiC. The complete assembly is shown in Fig. 5.2.

5.3 Experimental results

In our experiments, no cooling effect was observed for the irradiated silicon and graphite samples. The null result in silicon can be explained by the low density of magnetic moments, 3.2×10^{16} cm^{-3}, which is the lowest among all irradiated samples that were used in our experiments. The total accessible paramagnetic entropy of the irradiated silicon sample is 1.7×10^{-3} μJ/K in magnetic field of 1 T. On the other hand, the graphite sample has a much smaller physical size and thus does not have a sufficiently large paramagnetic entropy. The total paramagnetic entropy of the graphite sample is estimated to be $2.0 \times$ μJ/K in magnetic field of 1 T.

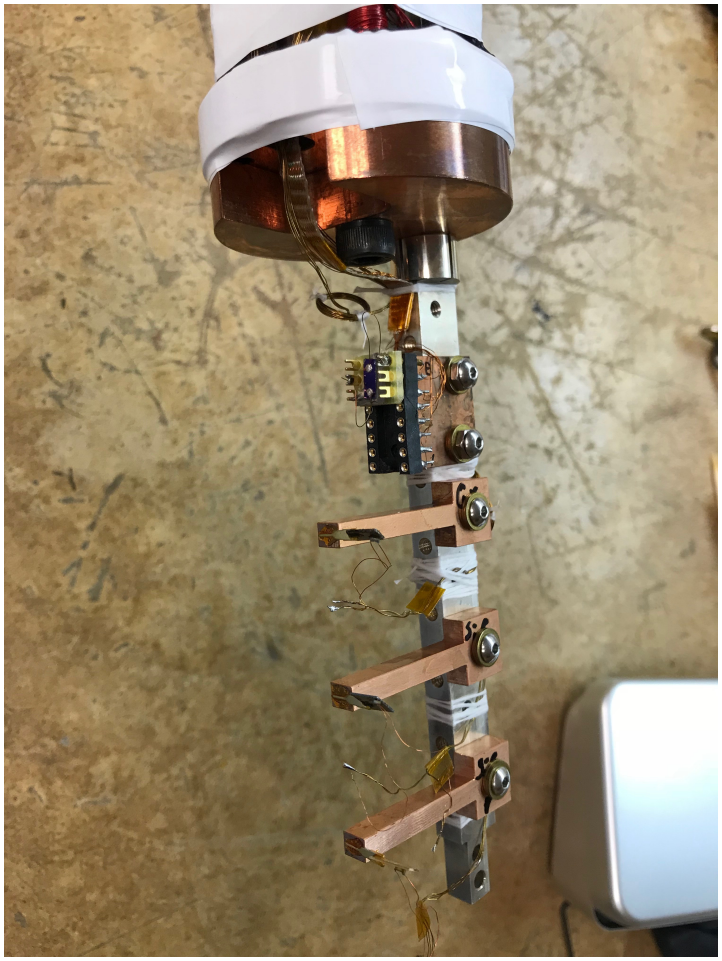

Figure 5.2: Mounting of irradiated samples investigated in the repeated experiment. Only samples of irradiated graphite and silicon carbide, as well as pristine silicon carbide are mounted (from top to bottom).

However, for irradiated silicon carbide, a much larger cooling effect than that which was found in Si:P in chapter 4 was observed. As a result, a wider magnetic field range was chosen for magnetic field sweeps since long-term temperature stability was less important in the presence of a larger temperature change signal. The field range was set from 0.2 T to 1.2 T, and the sweep rates were chosen to be 0.1, 0.05, and 0.025 T/min. As mentioned earlier, 0.1 T/min is the maximum rate admitted by the 8 T superconducting solenoid.

Fig. 5.3 shows the measured resistance of the RuO_x thermometers mounted on irradiated and pristine SiC during the experiment for a 0.1 T/min sweep rate. The resistance shows distinctly different behaviour for the two samples: the signal from the thermometer mounted on irradiated SiC shows a rapid step-like change when the direction of the magnetic field sweep is reversed while the pristine SiC shows no step-like changes at moments of field reversal. For a better demonstration of the effect, and to enable comparison to simulation, a transformation from thermometer resistance to temperature is required. It is known that a positive magnetoresistance is prominent in RuO_x in this temperature range, so before the temperature can be determined using a known calibration curve, the thermometer resistance must be corrected for its magnetoresistance. We assume a constant temperature for the pristine SiC sample during magnetic field sweeps, as well as a differential sensitivity dR/dT that is not affected by the applied magnetic field following the same reasoning as that in section 4.2.3. The resulting temperature values are shown in Fig. 5.4. In agreement with the model (eq. 4.1) developed in chapter 4, the temperature during a sweep up in magnetic field is higher than the temperature

during a sweep down in magnetic field. The observed heating and cooling is in agreement with that expected from manipulation of the paramagnetic entropy with the swept magnetic field.

To arrive at a quantitative analysis of the measured temperature versus time, a numerical solution of equation 4.1 was obtained. Such a solution has only two free parameters τ_{th} and $C_{parasitic}$ that can not be obtained from the published results and either has to be fitted or measured experimentally. The thermal time constant was taken to be $\tau_{th} = 8$ seconds from the fitting of corresponding T vs time dependency during a magnetic field sweep. One can stop a magnetic field sweep at some value and observe sample temperature exponentially reach an equilibrium temperature in the absence of cooling or heating in a varying magnetic field. The specific heat is $C_{total} = C_{parasitic} + C_{magn}$, with the magnetic specific heat C_{magn} calculated from first principles assuming a system of $g = 2$ spins with J = 1 given the sample dimensions and magnetic moments density. The parasitic specific heat $C_{parasitic}$, which includes specific heat of SiC itself, the thermometer as well as any thermally-coupled to SiC, was taken to be equal to 6 μJ/K to obtain a quantitatively similar behavior with experimental results. This value was found by simulation for various values of $C_{parasitic}$ and comparison of a simulated temperature difference on magnetic sweeps up and down in a field to a difference obtained in experiment. For comparison, $C_{magn} = 2.46$ μJ/K given the sample dimensions and spin density at a temperature of 700 mK and a magnetic field of 0.7 T. We should emphasize that $C_{parasitic}$ is the only parameter of the simulation that has to be fit and good agreement with the experimental results presented in

Fig. 5.5 was obtained.

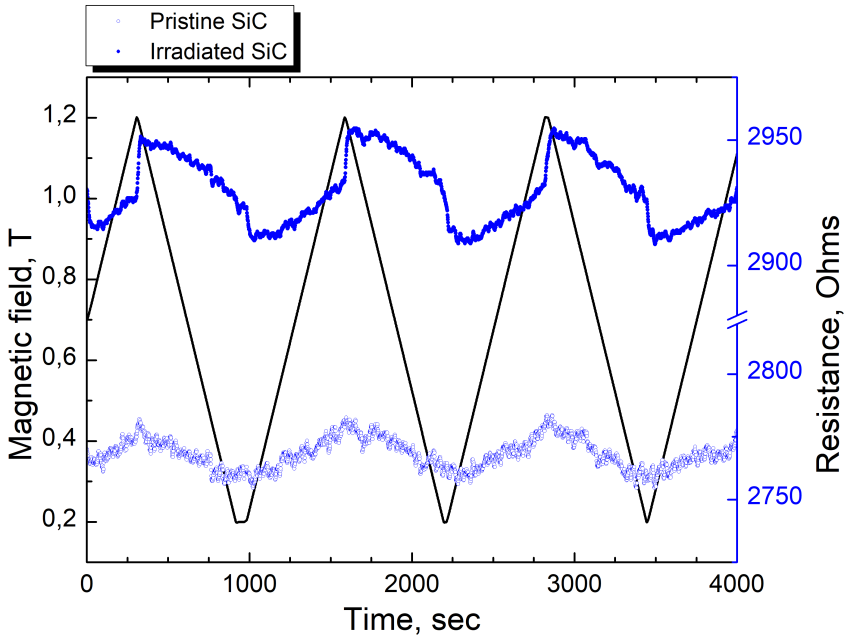

Figure 5.3: Measured resistance of RuO_x thermometers mounted on irradiated and pristine SiC samples during magnetic field sweeps.

Lower values of sweep rates were also tested. At a sweep rate of 0.05 T/min. A smaller temperature difference was measured for irradiated SiC on sweeps up and down of magnetic field. With a sweep rate of 0.025 T/min, the temperature change completely disappeared and was not observable with our temperature sensitivity.

As described previously in section 5.2, the experiment was repeated with a new design. The irradiated silicon was removed from the setup, and mechanical pressure was applied to the samples when they were being mounted to fork-shaped legs by VGE-7031 varnish. The modified mounting procedure brought the sample base temperature lower and the absolute temperature difference

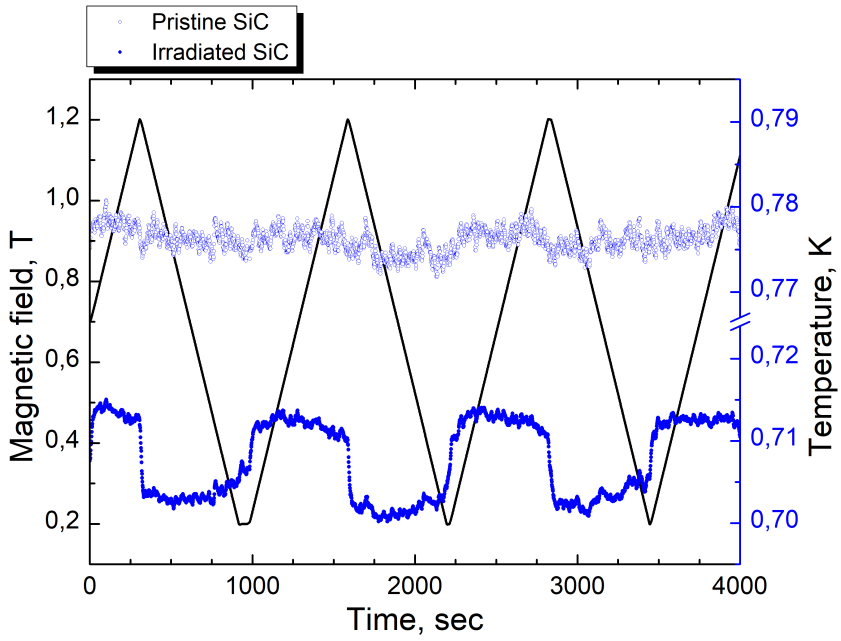

Figure 5.4: Temperature determined from RuO_x thermometers, after corrections for magnetoresistance.

between the irradiated and pristine SiC samples was reduced. A similar set of magnetic field sweep measurements was performed with the results shown in Figs. 5.6a and 5.6b. With the sample temperatures being closer to each other, a loop in temperature versus magnetic field is now a better visualization of the different behavior between irradiated and pristine silicon carbide samples. Here no additional correction of magnetoresistance was performed and the resistance reading from RuO_x thermometers was transformed to the temperature directly. Even though resistance reading are affected by the magnetic field, such change of resistance is the same for thermometers on both samples and it does not affect the comparison. No data correction was performed intentionally to emphasize that difference in behaviors of an irradiated and a pristine

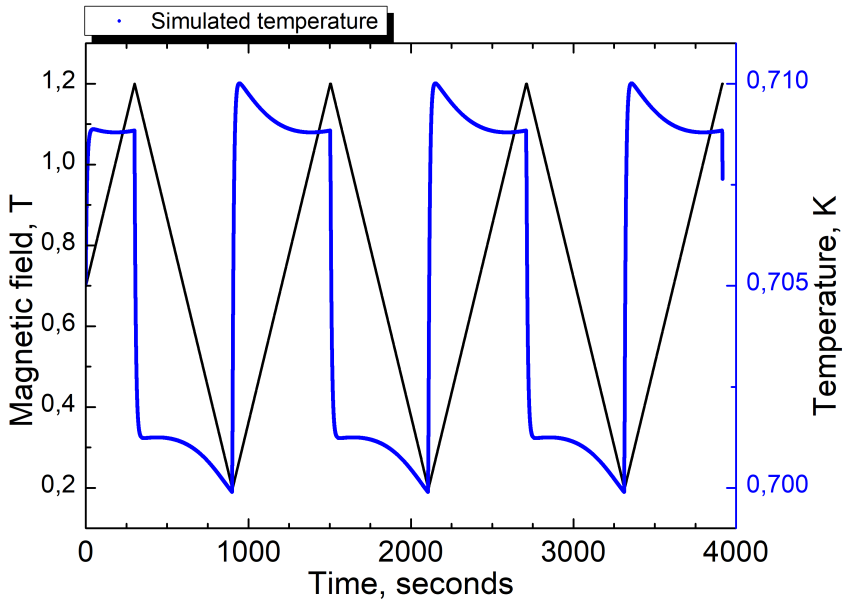

Figure 5.5: Simulated temperature evolution for an irradiated SiC sample during the magnetic field sweeps. Parasitic specific heat $C_{parasitic} = 6$ μJ/K, magnetic moments density $N_s = 5.3 \times 10^{19}$cm^{-3}, J = 1, g-factor = 2, sample dimensions are 4 mm x 3mm x 0.5mm, thermal time constant $\tau_{th} = 8$ seconds, magnetic field sweep rate 0.1 T/min.

SiC samples is not an artifact of a data processing. The deduced magnitude of the cooling effect for irradiated sample was determined to be 5.0 ± 1.8 mK.

5.4 Conclusion

A cooling effect was observed in an irradiated SiC sample, and there was an absence of cooling in a pristine SiC sample. The magnitude of the cooling effect is small, and is not yet practical for direct cooling applications. However, it does suggest a need for further investigation of other irradiated materials, most likely wide-gap semiconductors. The easy handling requirements, the produc-

(a)

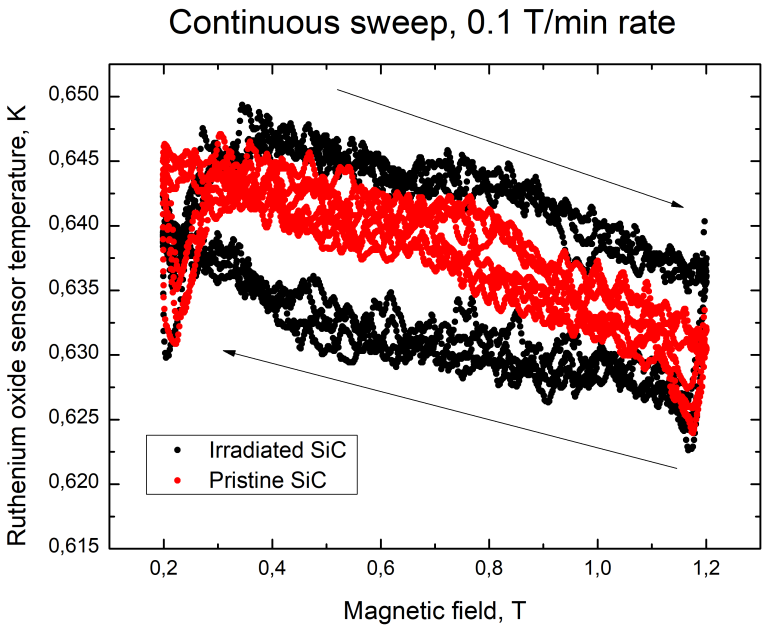

(b)

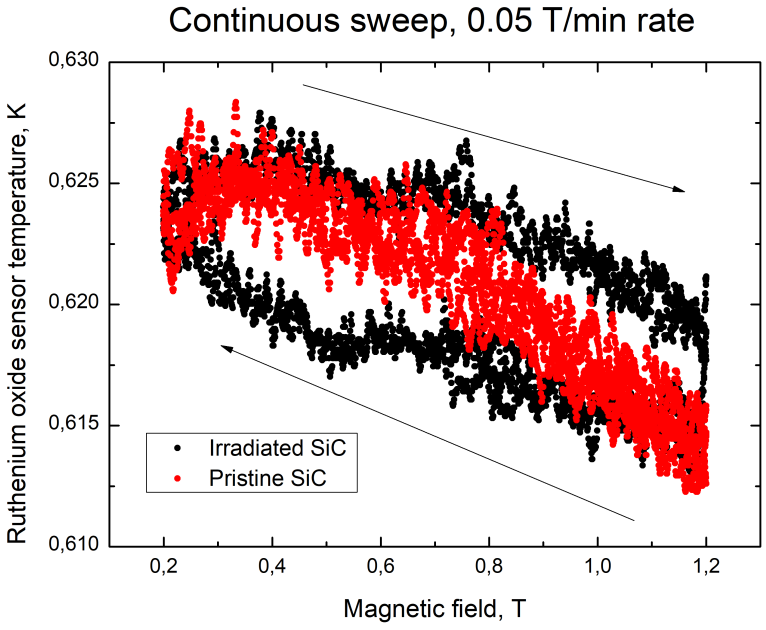

Figure 5.6: Measured temperature of pristine and irradiated SiC in repeated experiemnt with more homogenious thermal coupling to reservoir for both samples. a) The sweep rate is set to 0.1 T/min. b) The sweep rate is set to 0.05 T/min.

tion process and control of magnetic moment density by radiation exposure time could make this class of materials interesting for other low-temperature applications, such as a thermometry by way of magnetic susceptibility measurements.

Over the course of experimental research of neutron irradiated SiC 5 experiments were performed based on the number of data files that were used for data analysis.

6 G10 experiment

During an experiment related to the other materials discussed in previous chapters, a property of G10 garolite was "discovered". This material is widely used in cryogenics as a mechanical support and structure material in low-temperature parts due to its electrical insulating property and moderate thermal conductivity in the temperature range from 40 mK to 100 mK.

As a result, we found in a strong evidence for a cooling effect in G10 garolite when changing the magnetic field. This is particularly unusual since no direct evidence of magnetic properties of G10 was ever discovered in the literature. As such, a high magnitude of a temperature change signal during the experiment, in good agreement with the expected behavior (similar to other materials in this work, for which paramagnetic nature is definitely known), as well as the absence of other contributions as possible experimental artifact, suggest that G10 garolite is paramagnetic at temperatures down to 500 mK with a magnetic moments density on the order of 10^{19} cm^{-3}.

This result has important implications since G10 is an inexpensive commercially available material, it can withstand environmental cryogenic conditions,

it is easily machinable and as a result it is widely used in cryogenic applications. On the other hand, the currently wide existing adoption of this material without a more understanding of its magnetic properties, *i.e.* as sample holders, makes this newly discovered effect of cooling/heating having certain concerns regarding some previous works in the literature.

6.1 Original Si:As experiment by Guillemette *et al.*

In the original work of Jonathan Guillemette and co-workers [41], a hydrogenated graphene device was used as a low-temperature thermometer. A contacted piece of hydrogenated graphene was mounted on a piece of highly-conducting arsenic-doped silicon (Si:As). The silicon wafers were purchased from *Addison Engineering* and were degenerately doped with arsenic to a concentration range from 2 to 5×10^{19} cm^{-3}, equivalent to a resistivity on the range of $1 - 5$ m$\Omega \cdot$ cm. A picture of the device is shown in Fig. 6.1.

In the process of measuring the samples, a hysterisis-like loop during a relatively high-rate sweep was observed in the resistance, and it was attributed to a cooling effect of the underlying Si:As wafer. A typically observed curve is shown in Fig. 6.2. Even if the doping concentration of Si:As wafers in the original experiment was far from being optimal according to the model presented in Chapter 3, an attempt to replicate the result of the original experiment using thermometers with well-known properties was made in the present work.

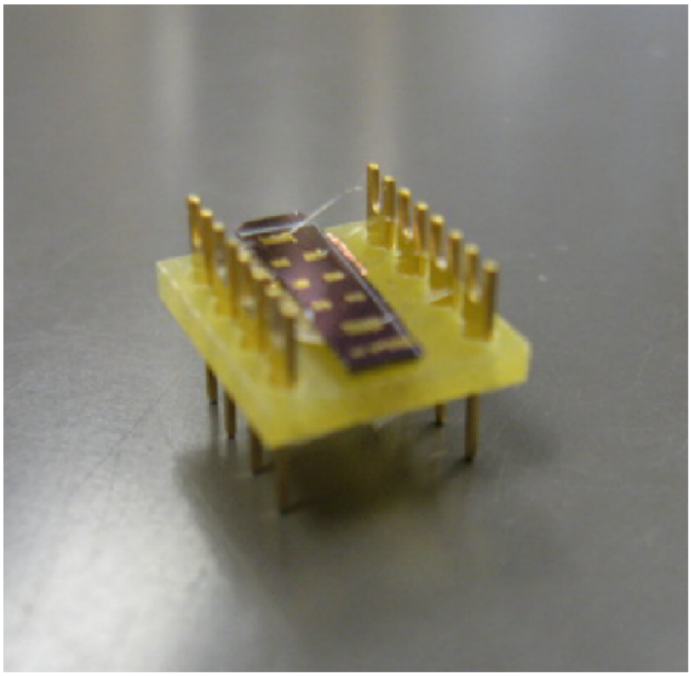

Figure 6.1: Typical hydrogenated graphene device on a G-10 chip carrier. From the original work of Guillemette *et al.* [41].

6.2 Attempt to reproduce Si:As experiment

In this thesis experiment, the same Si:As wafers from Addison Engineering were used. Parts of the wafers were cut to a shape approximately 1×3 cm in size and glued together using VGE-7031 varnish. The whole assembly was then put under force of approximately 10 N applied through the intermediate layer of high density foam for 24 hours and then glued to the same G10 sample carrier as a device from the original experiment.

This assembly was inserted into the 16 pin DIP socket sample holder, that in turn was glued to a mechanical mount made of G10 garolite. The mount was clamped to a silver rod well thermally anchored to the cold plate of a ^{3}He

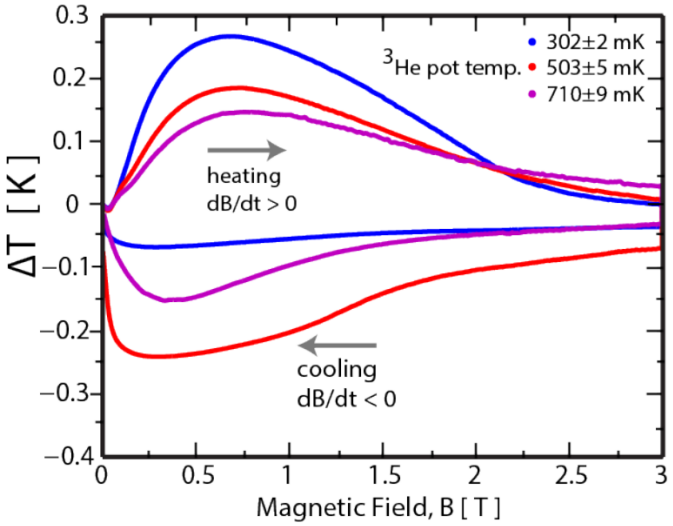

Figure 6.2: Typical loop on hydrogenated graphene device resistance during the fast magnetic field sweep. The sweep rate is 0.225 T/min (blue) and the steady state values as shown in red. From the original work of Guillemette *et al.* [41].

pot. A RuO_x thermometer was glued to the end of the assembly with VGE-7031 varnish. In the same 16 pin DIP socket, another carrier with a sample of irradiated silicon was placed together with another thermometer.

The experiment was placed in a cryostat and cooled to a base temperature of 330 mK according to the permanent built-in thermometer located on the ^{3}He plate. The magnetic field was swept in a range from 0.2 to 1.2 T at a rate 0.1 T/min.

Surprisingly, both thermometers showed a temperature response loop similar to what was found in the work of Guillemette *et al.* At first, it was attributed to the thermal contact through the 16 pin DIP sample holder however a subsequent experiment was immediately mounted with no irradiated silicon sample, as well as another RuO_x thermometer mounted on an empty

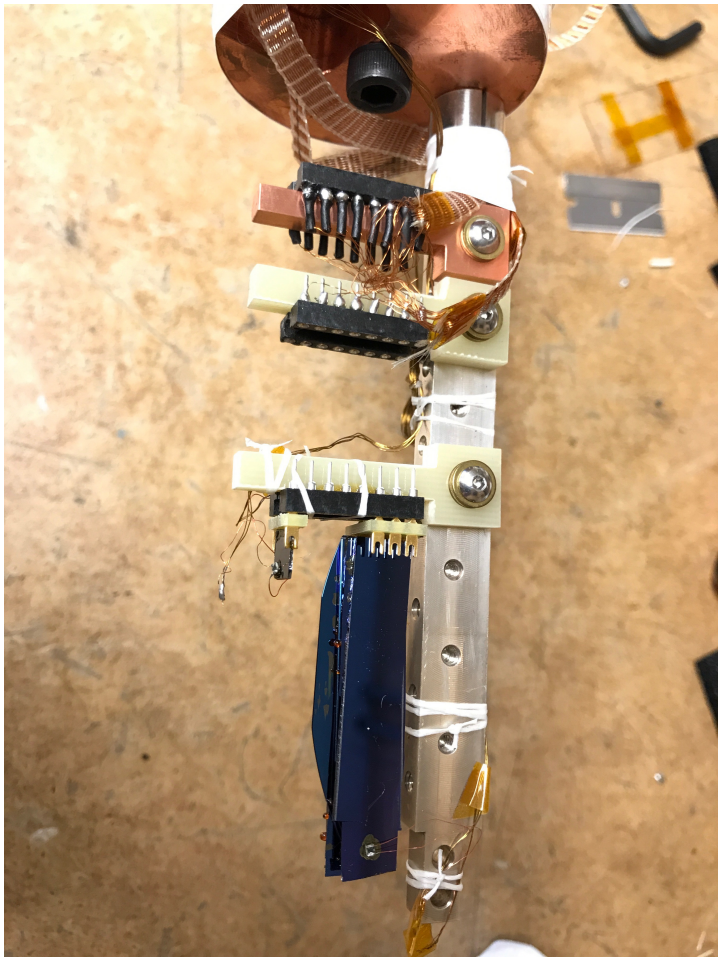

Figure 6.3: A stack assembled from highly-doped Si:As wafers mounted on a G10 sample carrier. The carrier is inserted into 16 pin DIP socket, itself glued on a G10 mechanical mount. The mount is clamped to a silver rod thermally anchored to the cold plate of ^{3}He pot of the cryostat. The empty 16 pin DIP socket is also shown.

G10 chip carrier, in the same way as can be seen on the Fig. 6.3. The magnetic field was swept in the same range and rate that was done previously. Surprisingly, it also showed a similar loop in the temperature response of the two thermometers. Such behavior suggested the need for a series of control experiments.

6.3 Control experiments with copper and G10 parts

The G10 mechanical mount is the piece with the largest mass (a non-sample parts) of the system. Therefore, it was decided to check its response in comparison with another identical mount, this one made out of copper. An individual RuO_x thermometer was glued to each mount using VGE-7031 varnish. The whole assembly is shown in Fig. 6.4. The experimental setup was located in a cryostat and cooled to the base temperature of 330 mK. The magnetic field was swept in the range of $0.2-1.2$ T, as was done previously, and at a rate 0.1 T/min. The temperature values from the RuO_x thermometers were recorded simultaneously during the sweep and they are shown in Fig. 6.5. Owing to the difficulty in making identical thermal contact between the G10 mount and a silver rod, the base temperatures of the two thermometers are non-identical. However, the one mounted on the G10 mount showed a larger temperature loop. This experiment indicated, at the very least, a need for further investigation of G10 garolite properties, a study that proved to be absolutely necessary.

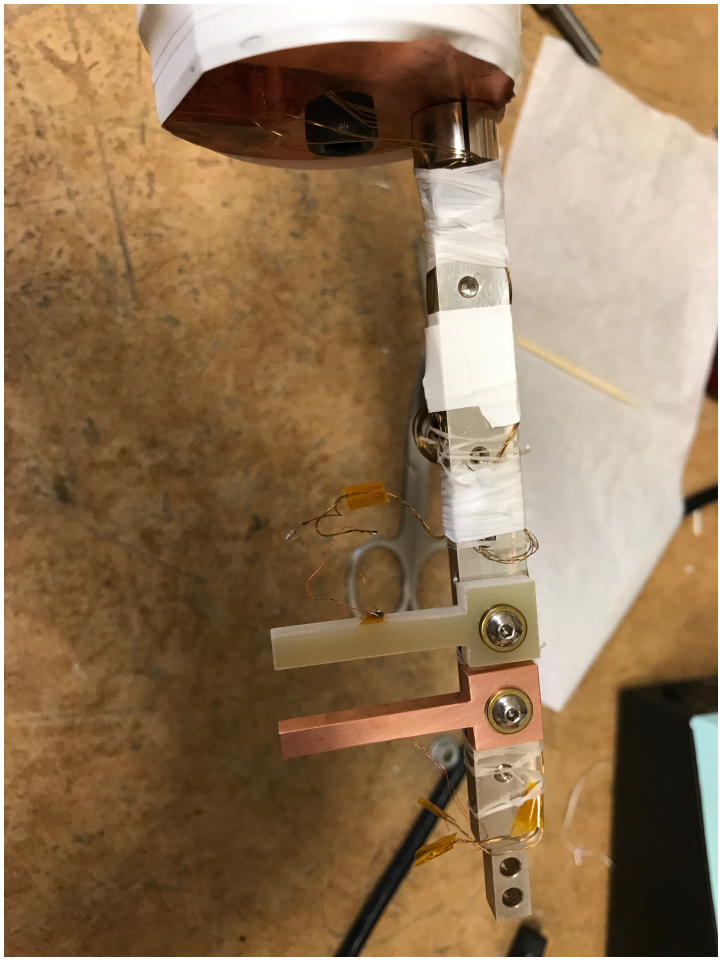

Figure 6.4: Two identical sample mechanical mounts made of copper and G10 garolite are clamped to a silver rod for the control experiment. An individual RuO_x thermometer is glued to each mount.

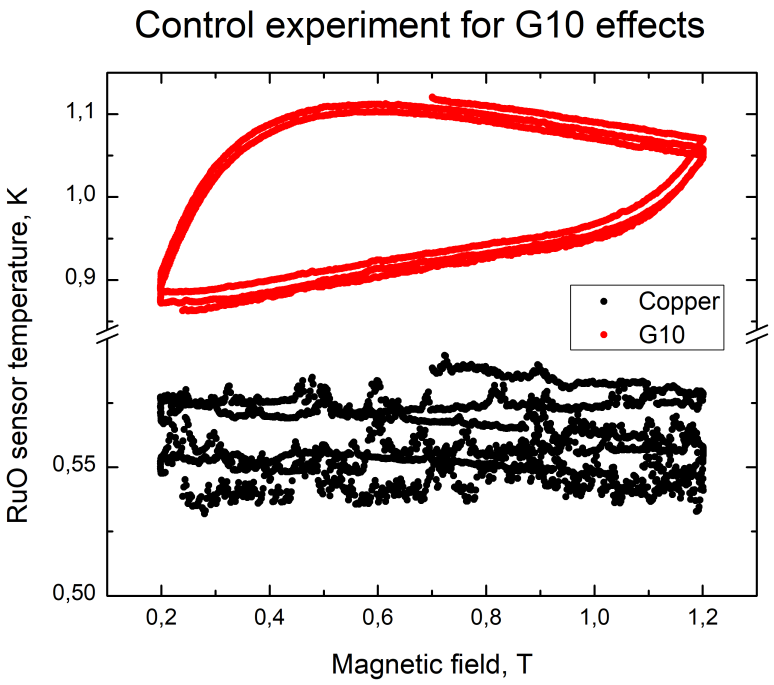

Figure 6.5: Temperature reading from RuO_x sensors placed on G10 garolite and copper mechanical mounts. Data taken simultaneously during the magnetic field sweep $0.2 - 1.2$ T with a 0.1 T/min rate.

6.4 Large G10 slab experiment design

A large plate of G10 garolite was purchased from McMaster-Carr with a 1" thickness and 6" $\times$ 6" lateral dimension. A rectangular bar with dimensions 1" $\times$ 1" $\times$ 5" was cut from it to fit into the cryostat vacuum chamber and was directly attached (glued) to the plate of the ^{3}He pot. On its other side, it was clamped by a thin G10 garolite plate supported between two M3 non-magnetic rods made of grade 316 stainless steel. Two RuO_x thermometers were glued close to the top and bottom of the bar and the wiring made as described in section 4.2.3. To investigate the possibility of a response arising from an

unusual thermometer behavior, a Cernox thermometer was also glued to the middle of the bar. The full assembly is shown in Fig. 6.6.

Figure 6.6: A large piece of G10 garolite glued and clamped to the ^{3}He cold plate.

The experimental setup was then mounted in a cryostat and cooled to the base temperature of 330 mK. The temperature of the sample itself was however 500 mK, per the measurement of another RuO_x thermometer mounted on the side of G10 bar closer to ^{3}He pot (referred further as the "bottom side" and "bottom thermometer" respectively). Unfortunately, the Cernox

thermometer was not calibrated and no standard reference curve was available from Lakeshore cryotronics.

6.5 Cooling efficiency

In this series of experiments, the same field range from 0.2 T to 1.2 T was chosen, as well as a set of sweep rates 0.1, 0.05, 0.25 and 0.01 T/min. The large mass and so the large specific heat of the G10 bar allowed to observe a loop in the temperature reading from the RuO_x thermometers even during a very small sweep rate. As mentioned before, 0.1 T/min is the maximum range allowed during the operation of the IceOxford Lemon system.

The set of cooling effect curves obtained is shown in Fig. 6.7. The size of the temperature loop consistently decreases with a decreasing rate for experiments with 0.05, 0.25 and 0.01 T/min rates. Meanwhile, a completely distinct shape of the loop in the experiment at the maximum sweep rate can be attributed to eddy current heating of the He^3 pot copper plate.

Fig. 6.8 shows the resistance values of a Cernox thermometer for various sweep rates. Cernox thermometers have negative differential sensitivity dR/dT, and so larger resistance values are obtained during sweeps with decreasing absolute value of the field. This indicates a consistency of the cooling effects observed in the RuO_x thermometers.

In addition, a sweep in a symmetric range ± 2 T was also performed as described in section 4.3. Here, the large specific heat of the sample allowed to overcome signals from parasitic heat releases happening in magnetic fields close to zero. Such symmetric sweep was only performed at the maximum

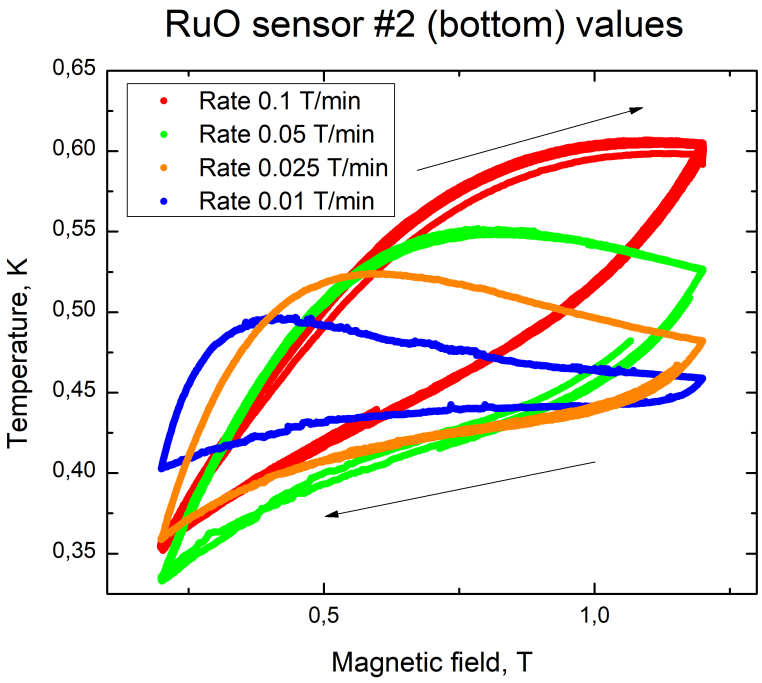

Figure 6.7: Demonstrated cooling effect for G10 garolite sample for various sweep rates. The arrows indicate the direction of the magnetic field along the curve.

sweep rate 0.1 T/min and the result is presented in Fig. 6.9. This behavior is consistent with the results expected from section 4.3, *i.e.* with the cooling curve being symmetric over $B = 0$ and the result from an original work of Guillemette *et al.* [41], and it is shown in Fig. 6.2.

To give a sense of similarity between the adiabatic cooling experiments, another sweep at a rate 0.1 T/min from 1.2 T to 0.2 T was performed, with the sample being cooled for 10 minutes after the initial field ramping to 1.2 T. This experiment also suggests a net cooling effect, with the sample temperature at 0.2 T being lower than 500 mK, the base sample temperature without field.

Fig. 6.10 shows all three steps of the process: cooling for 10 minutes in a

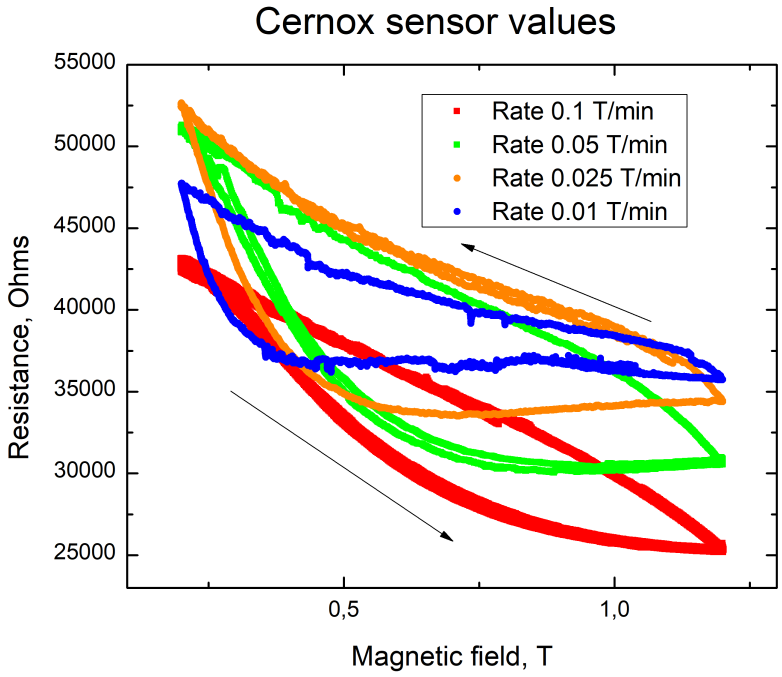

Figure 6.8: Resistance values of Cernox thermometer mounted on G10 garolite sample at various sweep rates. The arrows indicate the direction of the magnetic field along the curve.

1.2 T field after initial ramping, a continuous sweep at 0.1 T/min rate to 0.2 T followed by warming due to coupling to the cold plate of ^{3}He pot. The last step, the warming process, indicates that the sample temperature during the field sweep was lower than the value reachable simply by the thermal contact to the ^{3}He pot.

Fig. 6.11 shows the temperature values of the ^{3}He pot measured by a built-in Cernox thermometer during field sweeps from 0.2 T to 1.2 T, at a 0.1 T/min rate. There is no observable loop, and only the change of the temperature value due to a negative magnetoresistance of the thermometer is observed. This also suggests a loop size of 100 mK observed during the sweep shown on a Fig. 6.7,

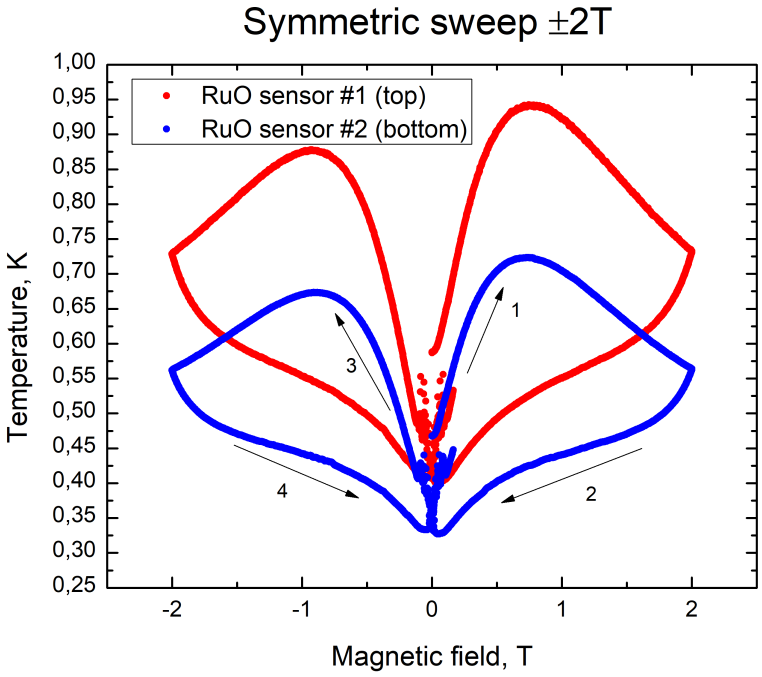

Figure 6.9: Continuous sweep in a symmetric range ±2 T suggests that the cooling/heating effect only depends on the value of $d|B|/dT$, as described in section 4.3.

and that it emanates from the G10 itself, and this is not a parasitic effect.

With the two RuO_x thermometers mounted in this experiment, a thermal boundary resistance R_{th} measurement was performed in the same way as described in section 4.6. A DC bias was applied though the resistor with a total heating power of 0.55 μW, resulting in a temperature change of 12.8 mK and a deduced boundary resistance 2.3×10^4 $\frac{\mathrm{K}}{\mathrm{W}}$.

The resulting heating/cooling effect magnitude, and derivations from section 4.3, allow us to estimate the spin density in the G10 garolite sample. For this estimate, an average cooling power at a sweep rate of 0.1 T/min and $B = 700$ mT was used with a corresponding temperature change of 100 mK.

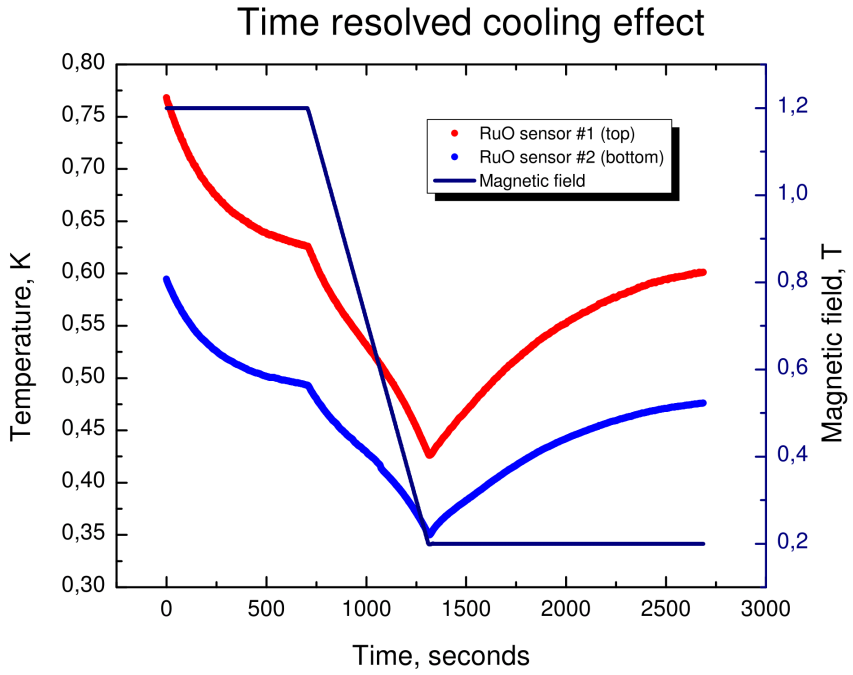

Figure 6.10: Continuous sweep from 1.2 T to 0.2 T at a 0.1 T/min rate after an initial cooldown at a maximum field value. A cooling effect of $\sim$ 120 mK is suggested by the data.

The resulting spin density is deduced to be $1.0 \times 10^{19}\text{cm}^{-3}$, assuming a system of $J = 1/2$ with $g = 2$.

Over the course of experimental research of G10 garolite 2 experiments with a small sample and 3 expeperiments with a large slab were performed based on the number of data files that were used for data analysis.

6.6 Conclusion

A cooling effect is found to likely occur in a sample made out of G10 garolite. Various experiments were performed to show that it was due to

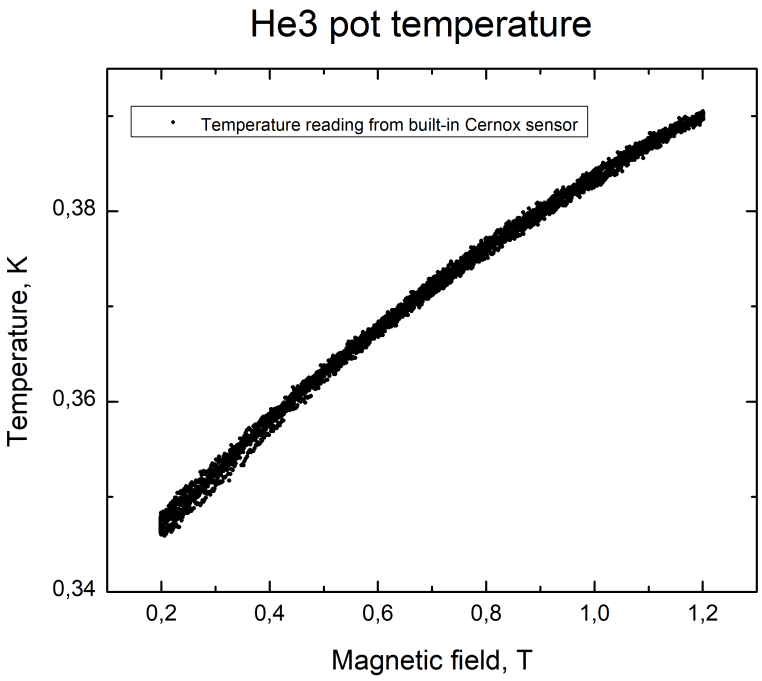

Figure 6.11: Temperature of ^{3}He pot measured by built-in Cernox thermometer during field sweeps from 0.2 T to 1.2 T at 0.1 T/min rate.

properties of the G10 itself rather than unexpected sources. The value of the cooling effect is the largest between all the materials studied in this work. It also indicates a need for further experiments and a deeper understanding of magnetic impurities in insulating materials.

To further (and independently) confirm the magnetic properties of G10 garolite, a direct magnetization measurement should be done. Such measurement would directly indicate the paramagnetic nature of the material and it would allow to estimate the density of magnetic moments N_s in the magnetic system.

7 Conclusion and Future Works

7.1 Summary of the main findings

An extensive search of new materials for adiabatic paramagnetic cooling was performed with the following results:

1. A model to evaluate the efficiency of materials for adiabatic paramagnetic cooling was developed.

2. A wide range of materials was considered under this model with projected performance published in a refereed journal [42].

3. A cooling effect in paramagnetically-doped semiconductor Si:P was experimentally demonstrated.

4. A cooling effect in the semiconductor SiC with paramagnetic properties induced by radiation was experimentally demonstrated.

5. A cooling effect in G10 garolite fiberglass was experimentally demonstrated with a substantial cooling effect.

The experimental work flow described in this thesis can be utilized in a wide set of cryogenic apparatuses and it allows relatively easy measurement to benchmark the performance of new material candidates during adiabatic cryogenic cooling.

7.2 Future work

The research conducted in this thesis leaves many questions, but also opens up new investigations. The future work may consist of:

1. Questions about magnetic properties of neutron irradiated highly oriented pyrolytic graphite (HOPG) remain open. Magnetic moments density from published work is very high for this material although no cooling effect was observed during our set of experiments.

2. Manganese doped GaN has magnetic moments density higher than commonly used paramagnetic salt CMN, one that makes it a good candidate for an attempt of experimental demonstration of the cooling effect.

3. Substantial cooling effect in G10 experiments opens a wide area for future work. Extension of temperature range to lower values could allow to further evaluate potential applications of this material for adiabatic paramagnetic cooling and thermometry at cryogenic temperatures. Direct magnetization measurements at temperatures below 4 K will allow to simultaneously evaluate all necessary quantities: density of magnetic moments, properties of magnetic moments (g-factor and J state) and ordering temperature.

4. The origin of the magnetic moments in G10 remains an important open question and research regarding the chemical composition of commercially available G10 garolite should be performed.

Appendices

In addition to investigation of the G10 properties in calorimetry experiments, direct measurements of magnetic properties were performed in collaboration with other researchers. The experiment described in this section was performed by our colleagues in Institute of Physics and Technology Russian Academy of Sciences (IPT RAS) in a vibrating magnetometer, in the temperature range from 4.2 K to 300 K.

The sample was cut from the same piece of G10 that was used in the calorimetry experiments. The sample dimensions are $l \times d \times h = 25.3 \times 3.8 \times 2.8\text{mm}^3$ and its mass is $m = 0.4694(2)$g. In a series of two experiments, first the data from mounted sample was obtained, and then an empty sample holder was measured as a background signal. The direction of applied magnetic field is perpendicular to $l \times d$ plane.

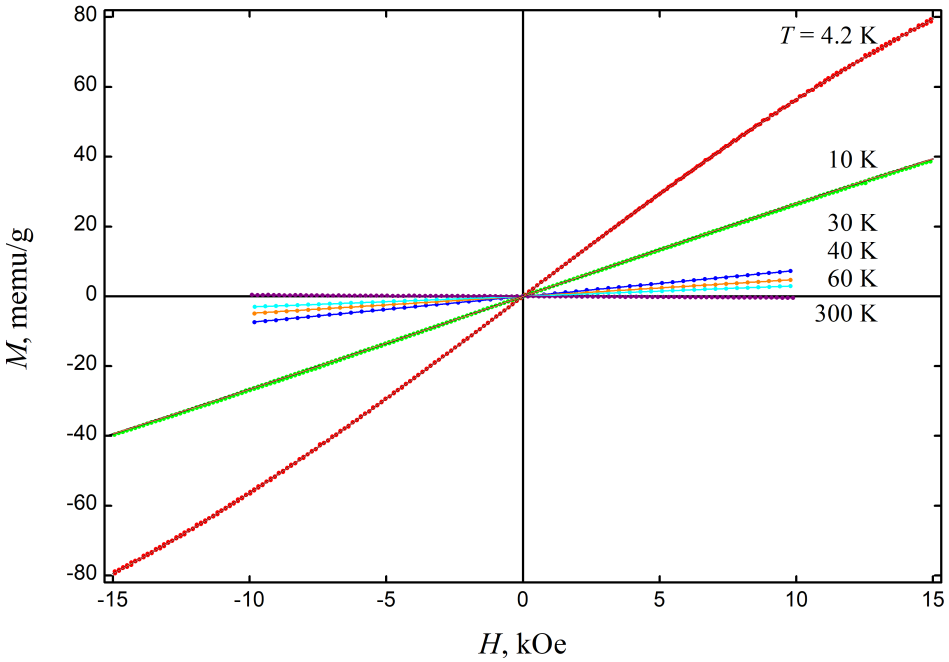

Figure A.1: G10 garolite magnetization measurements. At temperature below 60 K, the sample shows clear paramagnetic behavior.

The measurements are shown in Fig. A.1 with the background signal already subtracted. The final set of data was generously supplied by our colleagues from IPT RAS and is plotted as is. At temperatures below 60 K, the sample shows clear paramagnetic behavior. Unfortunately, a small magnetic field range and the inaccessibility of lower temperature values does not allow to demonstrate the expected saturation behavior.

References

[1]E. Warburg and L. Hönig, "Ueber die wärme, welche durch periodisch wechselnde magnetisirende kräfte im eisen erzeugt wird", Annalen der Physik **256**, 814–835 (1883).

[2]W. F. Giauque and D. P. MacDougall, "Attainment of temperatures below 1 ∘ absolute by demagnetization of $Gd_2(SO_4)_3{\cdot}8H_2O$", Phys. Rev. **43**, 768–768 (1933).

[3]F. Pobell, *Matter and methods at low temperatures* (Springer, New York NY, 1992).

[4]J. M. Hornibrook, J. Colless, I. D. Conway Lamb, S. J. Pauka, H. Lu, A. C. Gossard, J. D. Watson, G. C. Gardner, S. Fallahi, M. Manfra, and D. J. Reilly, "Cryogenic control architecture for large-scale quantum computing", **3** (2014).

[5]M. Mohseni, P. Read, H. Neven, S. Boixo, V. Denchev, R. Babbush, A. Fowler, V. Smelyanskiy, and J. Martinis, "Commercialize quantum technologies in five years", Nature **543**, 171–174 (2017).

[6]D. A. Shea and D. Morgan, `https://fas.org/sgp/crs/misc/R41419.pdf`, 2010.

[7]D. I. Bradley, A. M. Guénault, R. P. H. D. Gunnarsson, S. Holt, A. T. Jones, Y. A. Pashkin, J. Penttilä, J. R. Prance, M. Prunnila, and L. Roschier, "On-chip magnetic cooling of a nanoelectronic device", Scientific Reports **7** (2017) `doi:10.1038/srep45566`.

[8]C. Ciccarelli, R. P. Campion, B. L. Gallagher, and A. J. Ferguson, "Intrinsic magnetic refrigeration of a single electron transistor", Applied Physics Letters **108**, 053103 (2016).

[9]Oxford Instruments Plc., `https://www.oxford-instruments.com/`, 2017.

[10]H. P. R. Frederikse, "Thermoelectric power of germanium below room temperature", Phys. Rev. **92**, 248–252 (1953).

[11]H. J. Goldsmid, "Bismuth–antimony alloys", Physica Status Solidi (a) **1**, 7–r28 (1970).

[12]N. A. Sidorenko, "Thermoelectric materials for peltier cryogenic coolers", ICEC 14 Proceedings.

[13]S. R. Harutyunyan, V. H. Vardanyan, A. S. Kuzanyan, V. R. Nikoghosyan, S. Kunii, K. S. Wood, and A. M. Gulian, "Thermoelectric cooling at cryogenic temperatures", Applied Physics Letters **83**, 2142–2144 (2003).

[14]A. Bentien, S. Johnsen, G. K. H. Madsen, B. B. Iversen, and F. Steglich, "Colossal seebeck coefficient in strongly correlated semiconductor $FeSb_2$", EPL (Europhysics Letters) **80**, 17008 (2007).

[15]Y. Wang, N. S. Rogado, R. J. Cava, and N. P. Ong, "Spin entropy as the likely source of enhanced thermopower in $Na_xCo_2O_4$", Nature **423**, 425–428 (2003).

[16]J. Flipse, F. L. Bakker, A. Slachter, F. K. Dejene, and B. J. van Weess, "Direct observation of the spin-dependent peltier effect", Nature Nano **7**, 166–168 (2012).

[17]G. E. W. Bauer, E. Saitoh, and B. J. van Wees, "Spin caloritronics", Nature Materials **11**, 391–399 (2012).

[18]Marlow Industries Inc, `http://www.marlow.com`, 2011.

[19]T. Harman, "Theory of the infinite stage nernst-ettingshausen refrigerator", Advanced Energy Conversion **3**, 667–676 (1963).

[20]T. C. Harman, J. M. Honig, S. Fischler, A. E. Paladino, and M. J. Button, "Oriented single-crystal bismuth nernst-ettingshausen refrigerators", Applied Physics Letters **4**, 77–79 (1964).

[21]K. Scholz, P. Jandl, U. Birkholz, and Z. M. Dashevskii, "Infinite stage ettingshausen cooling in Bi-Sb alloys", Journal of Applied Physics **75**, 5406–5408 (1994).

[22]A. Pourret, K. Behnia, D. Kikuchi, Y. Aoki, H. Sugawara, and H. Sato, "Drastic change in transport of entropy with quadrupolar ordering in $PrFe_4P_12$", Phys. Rev. Lett. **96**, 176402 (2006).

[23]D. Jang, T. Gruner, A. Steppke, K. Mistumoto, C. Geibel, and M. Bando, "Large magnetocaloric effect and adiabatic demagnetization refrigeration with $YbPt_2Sn$", Nature Communications **6** (2015) 10.1038/ncomms9680.

[24]Y. Tokiwa, B. Piening, H. S. Jeevan, S. L. Budko, P. C. Canfield, and P. Gegenwart, "Super-heavy electron material as metallic refrigerant for adiabatic demagnetization cooling", Science Advances **2** (2016).

[25]M. Lakner, H. v. Löhneysen, A. Langenfeld, and P. Wölfle, "Localized magnetic moments in Si:P near the metal-insulator transition", Phys. Rev. B **50**, 17064–17073 (1994).

[26]A. G. Zabrodskii, "Magnetic ordering in doped semiconductors near the metal–insulator transition", physica status solidi (b) **241**, 33–39 (2004).

[27]A. Wolos, Z. Wilamowski, M. Piersa, W. Strupinski, B. Lucznik, I. Grzegory, and S. Porowski, "Properties of metal-insulator transition and electron spin relaxation in gan:si", Phys. Rev. B **83**, 165206 (2011).

[28]R. N. Bhatt and P. A. Lee, "Scaling studies of highly disordered spin 1/2 antiferromagnetic systems", **48**, 344–347 (1982).

[29]M. P. Marder, *Condensed matter physics second edition* (John Wiley and Sons Inc., Hoboken NJ, 2000).

[30]M. Stutzmann and D. K. Biegelsen, "Electron-spin-lattice relaxation in amorphous silicon and germanium", Phys. Rev. B **28**, 6256–6261 (1983).

[31]Y. Liu, R. Pan, X. Zhang, J. Han, Q. Yuan, Y. Tian, Y. Yuan, F. Liu, Y. Wang, A. T. N'Diaye, E. Arenholz, X. Chen, Y. Sun, B. Song, and S. Zhou, "Vacancy defect complexes in silicon: charges and spin order", Phys. Rev. B **94**, 195204 (2016).

[32]Y. Wang, P. Pochet, C. A. Jenkins, E. Arenholz, G. Bukalis, S. Gemming, M. Helm, and S. Zhou, "Defect-induced magnetism in graphite through neutron irradiation", Phys. Rev. B **90**, 214435 (2014).

[33]Y. Wang, Y. Liu, E. Wendler, R. Hübner, W. Anwand, G. Wang, X. Chen, W. Tong, Z. Yang, F. Munnik, G. Bukalis, X. Chen, S. Gemming, M. Helm, and S. Zhou, "Defect-induced magnetism in SiC: interplay between ferromagnetism and paramagnetism", Phys. Rev. B **92**, 174409 (2015).

[34]W. F. Giauque, R. A. Fisher, E. W. Hornung, and G. E. Brodale, "Magnetothermodynamics of Ce2Mg3(NO3)12 · 24H2O. i. heat capacity, entropy, magnetic moment from 0.5 to 4.2°k with fields to 90 kg along the a crystal axis. heat capacity of pyrex 7740 glass in fields to 90 kg", The Journal of Chemical Physics **58**, 2621–2637 (1973).

[35]M. Pawlowski, M. Piersa, A. Wolos, M. Palczewska, G. Strzelecka, A. Hruban, J. Gosk, M. Kamińska, and A. Twardowski, "Mn impurity in bulk gaas crystals", Acta Physica Polonica A **108**, 825 (2005).

[36]M. Zając, J. Gosk, M. Kamińska, A. Twardowski, T. Szyszko, and S. Podsiadło, "Paramagnetism and antiferromagnetic d–d coupling in GaMnN magnetic semiconductor", Applied Physics Letters **79**, 2432–2434 (2001).

[37]P. P. Edwards and M. J. Sienko, "Universality aspects of the metal-nonmetal transition in condensed media", Phys. Rev. B **17**, 2575–2581 (1978).

[38]G. Feher and E. A. Gere, "Electron spin resonance experiments on donors in silicon. ii. electron spin relaxation effects", Phys. Rev. **114**, 1245–1256 (1959).

[39]N. Kobayashi, S. Ikehata, S. Kobayashi, and W. Sasaki, "Specific heat study of heavily P doped Si", Solid State Communications **24**, 67–70 (1977).

[40]S. Wagner, M. Lakner, and H. v. Löhneysen, "Specific heat of Si:(P,B) at low temperatures", Phys. Rev. B **55**, 4219–4224 (1997).

[41]J. Guillemette, "Electronic transport in hydrogenated graphene", PhD thesis (Department of Physics, McGill University, Montréal, Québec, Canada, 2014).

[42]A. Vlasov, J. Guillemette, G. Gervais, and T. Szkopek, "Magnetic refrigeration with paramagnetic semiconductors at cryogenic temperatures", Applied Physics Letters **111**, 142102 (2017).

[43]C. Kittel, *Introduction to solid state physics* (Wiley, Hoboken NJ, 2005).

[44]Intel Inc, `https://newsroom.intel.com/news/intel-delivers-17-qubit-superconducting-chip-advanced-packaging-qutech/`, 2017.

[45]D-Wave Systems Inc, `https://www.dwavesys.com`, 2017.

[46]D. S. Betts, "Pomeranchuk cooling by adiabatic solidification of helium-3", Contemporary Physics **15**, 227–247 (1974).